From Materials to Devices:

(I) Ultrathin Flexible Implantable Bio-probes with Biodegradable Sacrificial Layers

(II) Carrier Spin Injection and Transport in Diamond

by

Xiangbing Jiao

A Dissertation Presented in Partial Fulfillment
of the Requirements for the Degree
Doctor of Philosophy

Approved March 2018 by the
Graduate Supervisory Committee:

Quan Qing, Co-Chair
Terry Alford, Co-Chair
Robert Nemanich

ARIZONA STATE UNIVERSITY

May 2018

ABSTRACT

My research has been focusing on the innovations of material and structure designs, and the development of fabrication processes of novel nanoelectronics devices.

My first project addresses the long-existing challenge of implantable neural probes, where high rigidity and high flexibility for the probe need to be satisfied at the same time. Two types of probes that can be used out of the box have been demonstrated, including (1) a compact probe that spontaneously forms three-dimensional bend-up devices only after implantation, and (2) an ultra-flexible probe as thin as 2 μm attached to a small silicon shaft that can be accurately delivered into the tissue and then get fully released in situ without altering its shape and position as the support is fully retracted. This work provides a general strategy to prepare ultra-small and flexible implantable probes that allow high insertion accuracy and minimal surgical damages with best biocompatibility.

My second project focuses on the injection and characterization of carrier spins in single crystal diamond based nanoscale devices. The conventional diamond-based quantum information process that exploits nitrogen vacancy centers faces a major barrier of large scale communication. Electron/hole spin in diamond devices, on the other hand, could also be a good candidate for quantum computing due to the very small spin-orbit coupling and great coherent transport length of spin. To date, there has been no demonstration of carrier spin transport in diamond. In this work, I try to answer this fundamental question of how to inject and characterize electron spins in Boron doped diamond. Nanoscale diamond devices have been fabricated to investigate this question, including Hall bar device for material characterization, and lateral spin valve for injecting

spin-polarized current into a mesoscopic diamond bar and detecting induced pure spin current. The preliminary results show signatures of spin transport in heavily doped diamond films.

Looking into the future, the knowledge we obtained in these two projects, including the strategy to integrate thin-film nanoelectronics devices on a flexible bio-probe configuration, and how to build spintronic devices with diamond structures, could be unified in the exploration of spin-based sensors in biological systems.

ACKNOWLEDGMENTS

I would like to express my deepest gratitude to my advisor, Dr. Quan Qing, who has guided me with his exceptional intelligence and generosity. He is not only an uncommonly nice and intelligent advisor, but also my role model. Without his guidance and support, this PhD research would not have been achievable. I am proud to be a student of Qing group. I would also like to express my great appreciation to my committee co-chair, Dr. Terry Alford, and committee member, Dr. Robert Nemanich for their invaluable advices, insightful comments, and encouragement. In addition, I would like to thank Dr. Tingyong Chen for Hall Effect and spin signal measurements in diamond spintronics research.

My sincere thanks also go to my colleagues Ching-Wei Tsao, Houpu Li, Yuan Wang, Joshua Sadar, and Minxi Hu. I also want to thank Dr. Yu-Peng Lu and Dr. Guoqun Zhao from Shandong University for their endless support. I owe special thanks to my family for their unconditional love, and wish everyone good health.

I gratefully acknowledge the funding support by the National Institute of Biomedical Imaging and Bioengineering of the National Institutes of Health, and by the Air Force Office of Scientific Research.

TABLE OF CONTENTS

Page

CHAPTER Page

LIST OF TABLES

Table Page

LIST OF FIGURES

Figure Page

1. INTRODUCTION

Implantable probes have enormous applications in neural science research, biomedical diagnostics, and disease treatment. They have been used as the central unit for nerve excitation, action potential recording, and ultimately understanding brain functioning. A considerable amount of work has been dedicated to the innovation of material and structure designs for implantable probes. In general, the commercialized implantable probes are categorized into rigid and flexible types. The rigid probes are made of hard materials, e.g. metal wire or silicon, and are suitable for accurate positioning into tissue. However, the mechanical mismatch between soft tissue and rigid probe results in tissue reactions and micro-motions after surgery, which eventually leads to signal degradation. On the other hand, the flexible thin-film probes can conform to the surface of tissue to avoid the implantation lesion and micro-motions relative to the tissue. The major challenge of flexible probes is that they can only contact with the outermost surface of the organs so that it is difficult to acquire signals from areas deep below the surface. Existing improvements in probe design can address some of the constraints but typically not all of the constraints without resulting in limitations in abilities, or bringing additional complexities in assembly and surgery. To address this challenge, this dissertation presents two types of ultra-small flexible bio-probes that allow the highly accurate insertion with the best biocompatibility utilizing biodegradable sacrificial layers. One device design has flexible electrode structures that can spontaneously form three-dimensional shapes in situ after implantation. Another device design is a completely flexible film probe as thin as 2 μm attached to a small silicon shaft that can be precisely

delivered into the tissue and fully released in situ. The silicon shaft can then be fully retracted, leaving only the top thin film probe with its accurate shape and position in the tissue. This system provides new strategies to construct highly biocompatible ultra-small implanted electronic platforms with minimal surgical damages and makes a significant impact on biomedical research, diagnostics, and treatments.

Diamond, the unique material that exhibits superior mechanical, optical and electronic properties, has attracted extensive attention as an outstanding candidate for spintronics devices which could open new opportunities for developing next-generation. It has been proved that the nitrogen-vacancy (NV) centers in diamond can be addressed using conventional optical techniques. Also, the diamond defect centers have long spin coherence time at ambient temperatures, whereas other quantum computing systems are limited to cryogenic temperature. These properties make diamond suitable for quantum information processing and the diamond based small-scale quantum information processing utilizing NV centers has already been demonstrated. However, large-scale quantum computing in diamond still faces a major challenge of communication between the spin states of a large number of NV centers. For this purpose, carrier spin transport has been proposed. Diamond is expected to be an ideal material for spin transport because of its small spin-orbit coupling and long spin relaxation time. The demonstration of spin injection in diamond has not been realized to date as a result of difficulties in growing high purity diamond and nanofabrication on the diamond substrate. In this project, high-quality B-doped single-crystal diamond layers were epitaxially grown on (100) diamond substrate using microwave plasma chemical vapor deposition. Nanoscale diamond devices, including lateral spin-valves for spin injection and transport as well as

Hall bars for material characterization, were fabricated by electron beam lithography technique. The devices were characterized both at room temperature and 4.5 K. The preliminary results show signatures of spin transport that are observed in heavily doped diamond films.

In this dissertation, Chapter 2 is dedicated to ultrathin flexible implantable probes. The first section gives a literature review of implantable probes. Section 2.2 explains material and structure designs of the proposed probes. Key considerations of probe designs are analyzed, including supporting structure and material, biodegradable sacrificial layer for releasing flexible core functional electrodes, dissolution of the sacrificial layer, and fabrication procedures. Section 2.3 focuses on characterizations of Mg biodegradable sacrificial layer. First, the dissolution time and shelf-life are examined. The dissolution effect on cell viability and neuron excitability are then estimated by *in vitro* neuron and astrocytes viability test and patch clamp experiments. Finally, the immune response is evaluated using *in vitro* proliferation rate test. The following section 2.4 presents the fabrication and assembly of Type-I probe. It begins with the basic structures and analysis of the core bend-up electrodes, followed by cell stimulation test and detailed fabrication steps. In section 2.5, the Type-II probe structure, implantation procedures, thin-film integrity examination during implantation, and fabrication procedures are explained in detail. A conclusion on implantable probe project is made in section 2.6. Future work based on this project is proposed in section 2.7. Part of this chapter was published as Scalable Fabrication Framework of Implantable Ultrathin and Flexible Probes with Biodegradable Sacrificial Layers in Nano Letters (Jiao et al., 2017) (see appendix for co-authors agreement on using published work). The literature review

(page 6-10 and Figure 1-3) and discussion on future work (section 2.7) in this dissertation were added to the original published work.

Chapter 3 focuses on spin injection and transport in diamond. Section 3.1 gives an overview of spintronics and spin-based quantum computing. Next, section 3.2 explains the principles of injection and detection of carrier spins in doped diamond. Design and fabrication procedures of Hall bars and spin-valve devices are presented in section 3.5. The preliminary results are analyzed in section 3.6, including Hall bar characterizations, diamond conductivity calculation, Hall voltage and magnetoresistance recording, spin-valve devices characterizations, and spin-signal analysis.

Finally, a conclusion on the entire material and structure innovation for nanoelectronics is made in Chapter 4.

2. ULTRATHIN FLEXIBLE IMPLANTABLE PROBES

2.1 Introduction

For long-term biocompatibility and performance, implanted probes need to further reduce their size and mechanical stiffness to match that of the surrounding cells, which, however, makes accurate and minimally invasive insertion operations difficult due to lack of rigidity and brings additional complications in assembling and surgery. Here, we report a scalable fabrication framework of implantable probes utilizing biodegradable sacrificial layers to address this challenge. Briefly, the integrated biodegradable sacrificial layer can dissolve in physiological fluids shortly after implantation, which allows the in situ formation of functional ultrathin film structures off of the initial small and rigid supporting backbone. We show that the dissolution of this layer does not affect the viability and excitability of neuron cells in vitro. We have demonstrated two types of probes that can be used out of the box, including (1) a compact probe that spontaneously forms three-dimensional bend-up devices only after implantation and (2) an ultraflexible probe as thin as 2 μm attached to a small silicon shaft that can be accurately delivered into the tissue and then get fully released in situ without altering its shape and position because the support is fully retracted. We have obtained a >93% yield of the bend-up structure, and its geometry and stiffness can be systematically tuned. The robustness of the ultraflexible probe has been tested in tissue-mimicking agarose gels with <1% fluctuation in the test resistance. Our work provides a general strategy to prepare ultrasmall and flexible implantable probes that allow high insertion accuracy and minimal surgical damages with the best biocompatibility.

Implantable probes are microstructures implanted into animal or human tissue to serve as a communication bridge between biological neural tissues with external devices. They have been widely used for biomedical research, diagnostics and therapy, including neuro signal recording, neuromodulation, brain-machine interface (BMI), etc.[1-3] For example, deep brain stimulation probes have been used for the treatment of brain disease like Parkinson's disease since late 1980s.[4-7] Bilateral deep-brain stimulation around 150 Hz of subthalamic nucleus or the globus pallidus pars interna by implanted electrodes leads to patients' motor function improvement. [8] Other than direct electrical stimulation, probes can also be used for precise drug delivery and neural depth recording simultaneously in brain.[9] In addition, implantable probes have significantly enhanced basic electrophysiology studies. An important application in neuroscience is the development of BMI.[8,10] The effort into building direct function interfaces between brains and external devices started in 1970s when people seeks voluntary control over alpha rhythm.[11] At the end of twentieth century, researchers managed to control a robot arm in real-time using rat neurons recorded by arrays of electrodes.[12] The first success in clinical BMI application was achieved in 2006.[13] An Utah probe, which is discussed somewhere else in this thesis, was implanted in primary motor cortex to restore hand mobility. Neuronal signals recorded by the Utah probe were decoded and successfully operated devices.

Overall, there are two categories of commercialized probes that have been used in implantation. First, rigid microscale electrodes, including twisted microwires, tungsten microelectrodes, Michigan probes and Utah probes,[14-17] are most widely used when accurate positioning into the tissue are required. The major challenge for the chronic use

of these probes is the tissue reaction and scar formation around the probe due to the huge mechanical mismatch with the tissue, and micromotions relative to the tissue after the implantation, such that the active cells tend to migrate away from the implanted electrodes, which eventually leads to significant degradation of performance.[18-20]

The research work on developing rigid implantable probe can be traced back to the use of metal wire electrodes for electrical activity recording in the 1950s. The metal wire electrodes have simple structures, including a platinum or iridium wire, typically no more than 100 μm in diameter, and insulating layer.[21] The wire tip is exposed to serve as the recording site.[22,23] (See Figure. 1) Such electrodes can be easily fabricated by dipping metal wire in base solution to form the tapered structure and then coating the wire with insulating materials such as Parylene-C, polyimide, or Teflon.[2] The exposed recording site at wire tip can be formed by non-thermal ablation, laser machining, or direct exposure of scanning electron microscope (SEM) electron beam.[24] Multiplexed recording can be achieved by gluing multiple electrodes together to form an electrode bundle. However, they are too bulky for insertion into small area of brain. At the same time, the high Young's modulus and rigidity result in mechanical mismatch with soft tissue.

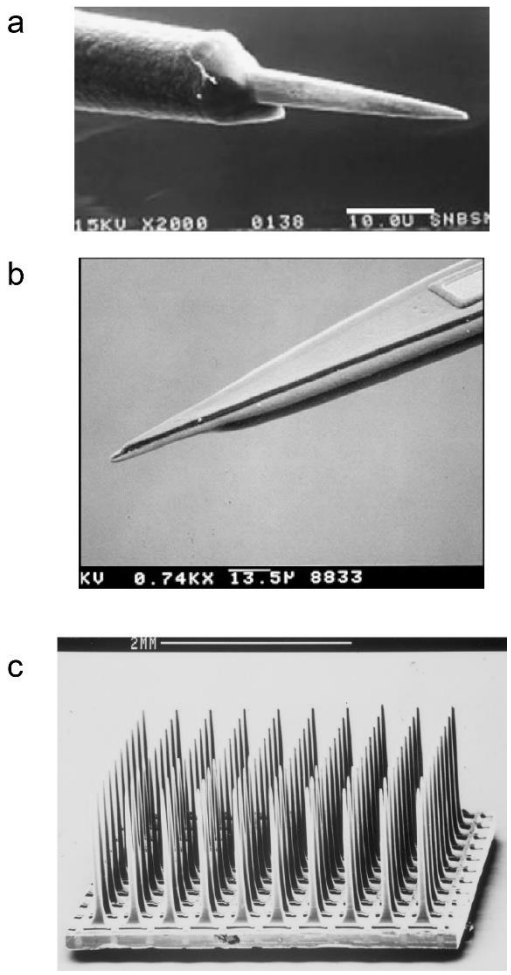

Figure 1. Rigid type implantable probes. (a) SEM image of metal wire electrode. The electrode is insulated by the 3 μm-thick Parylene-C layer. The exposed tip is prepared by laser ablation.[24] (b) Perspective view of a Michigan probe made by boron etch.[25] (c) SEM of Utah array.[15]

Another commonly used rigid probe is based on Silicon. The significant development in silicon micromachining greatly promoted the probe fabrication techniques. The invention of Michigan probe serves as a hallmark of micro machined probes. (see Figure. 1) Michigan probe typically comprises a silicon shaft and integrated metal electrodes, which are insulated by high-dielectric constant materials. The probe is

fabricated by a series of micromachining processes including lithography, metallization, anisotropic etch of silicon. The success of Michigan probe has attracted significant amount of interest in neural studies and implantable probe development. Another milestone on rigid type probe was the invention of Utah array. It consists of sharpened silicon probe array, whose tips are coated with metal for recording and stimulation. Compare to Michigan probe whose low mechanical strength causes crack and shatter during insertion, the electrode columns in Utah probe provide better rigidity that prevents electrodes from breaking. Although rigid type probes are proven successful tool for implanted neuro recording, the huge mechanical mismatch between the inserted probe and biological tissue that can cause tissue reaction, scar formation, and signal degradation, dramatically hinders its chronic recording ability.

The second type of implantable probe, known as flexible type probe, is based on soft materials. The flexible thin-film probes are used where they can conform to the shape of the tissue/organ so that it could bring less irritation to the live cells and better biocompatibility.[26-30] For example, as illustrated in Figure 2, a skin-like sensor made of gold electrodes and polyimide dielectric substrate and encapsulation layers offers outstanding flexibility and stretchability. This device can be mounted directly on human skin to sense electromyography or control prosthetic.[31] Figure 2 (b) shows another example of flexible implantable electrodes. This organic material-based sensor array can record local field potential as well as superficial neuron action potentials. It can conform to the surface of tissue, thus forming better interface with cell and improved signal qualities. However, the flexible type devices typically can only get in touch with the outmost surface of the tissue, and it is generally difficult to deliver the flexible structure

deep below the surface to get closer to the active cells, which reduces the resolution and quality of signals.

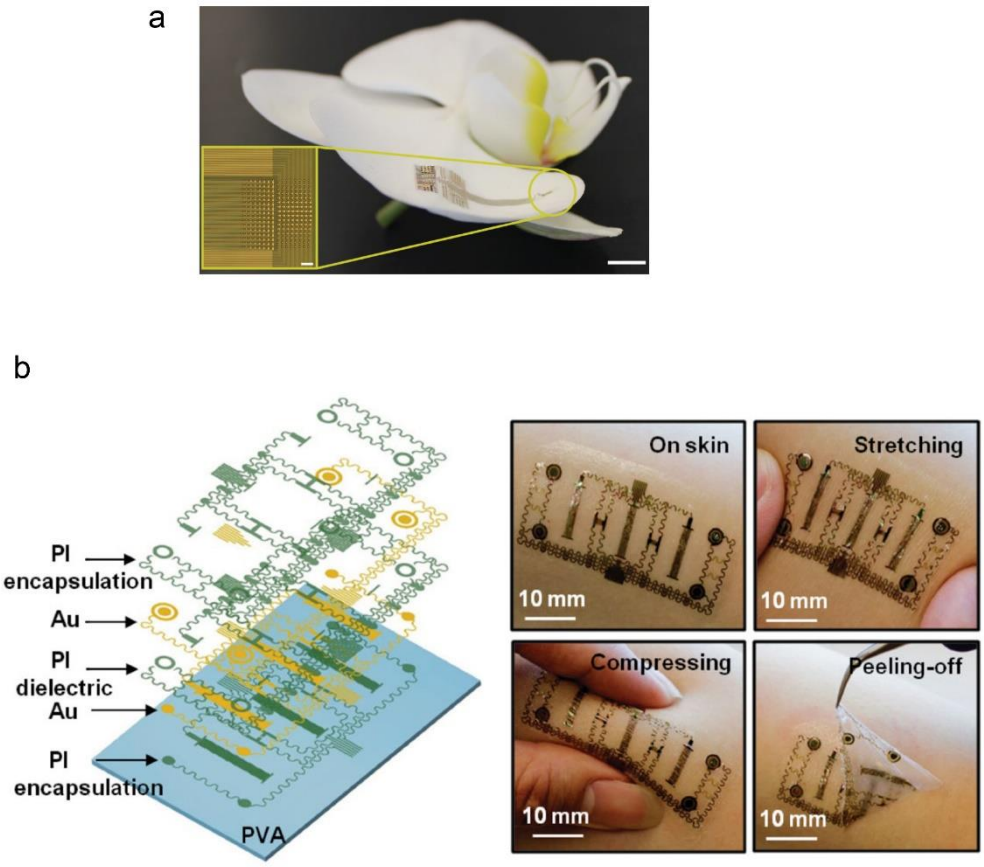

Figure 2. Flexible type probes. (a) The NeuroGrid, an all-flexible implantable electrode, conforms to the surface of an orchid petal. Scale bar, 5 mm. (b) Images of an epidermal stimulation and sensing platform made of Au electrodes and polyimide.

Recent advances in nano-bioelectronics and bioresorbable electronics have triggered a new wave of innovations of how to interface artificial devices to live cells and tissues.[32-37] For example, silicon nanowire based active nanoFET sensors,[26, 38-40] vertical

nanowire electrode arrays,[41-43] and silicon nanobelt devices[44] brings higher sensitivity, smaller size and stronger interaction with cells.[43, 44]

Furthermore, several new strategies have been explored to package nanomaterial-enabled devices in flexible forms and to deliver them inside tissue versus just to make a surface contact (see Figure 3).[45-54]

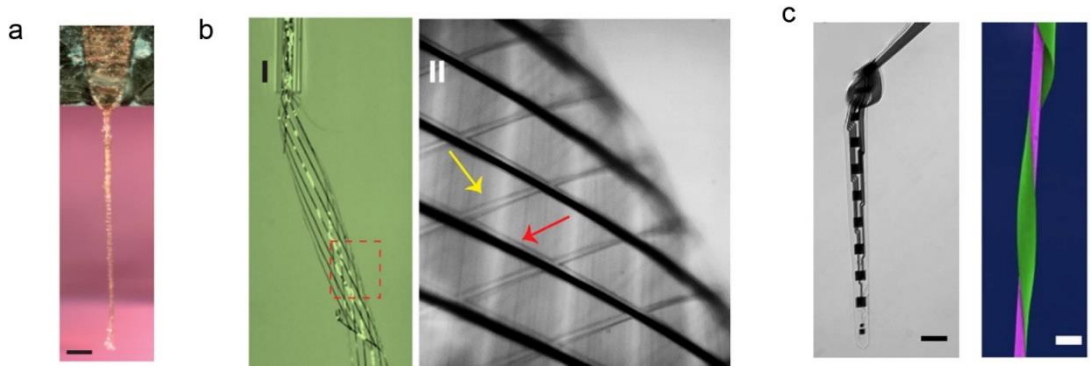

Figure 3. Delivery of flexible electronics inside tissue. (a) Nanoelectronic network in frozen state for insertion. Scale bar, 500 μm.[47] (b) Syringe-injectable electronics. Left: Injection of mesh electronics through a glass syringe. Right: Zoom-in view of the mesh electronics. Red and yellow arrows indicating polymer/metal interconnect, and transverse polymer element, respectively.[49] (c) Ultra-flexible nanoelectronic probe that can be implanted with the aid of a carbon fiber or tungsten wire insertion shuttle.[54] Left: A probe suspended in water. Scale bar, 50 μm. Right: SEM images (false-colored) of a probe (green) attached to a 20 μm tungsten shuttle (purple). Scale bar, 50 μm.

Specifically, Xie et al. developed procedures to implant three-dimensional ultra-flexible macroporous nanoelectronic probes into the brain shortly after freezing the probes in liquid nitrogen so that the rigidity of the probes is temporarily strong enough to penetrate the tissue before thawing in position.[47] In addition, Liu et al. and Hong et al.

have recently demonstrated injectable flexible electronics into tissues, in which packed microporous mesh electronics is directed through a syringe by a flux of liquid, and multiplexed connection can be made using conductive ink printing technique.[48, 49] This technique enables the delivery of large area network of devices with high yield into hidden or opaque regions with the aid of field of view control. The device mesh typically forms a cylinder with a diameter of a couple of hundred μm up to mm as the soft probes need to be first separated from the fabrication substrate, and then delivered as suspended in medium. Significantly, Zhou et al. showed recently that such highly porous structure could lead to much less inflammation and damage to surrounding neurons and no chronic immune response nor negative effect on the natural distribution of neurons.[50] On the other hand, Hwang et al. proposed transient electronics for implanted application which utilizes biodegradable materials, also known as bioabsorbable materials that are soluble in aqueous solutions or biofluids, specifically for functional components, connection wires and packaging, and the whole circuit will be absorbed by the tissue and disappear after an extended period.[51] In addition, for the implantation of ultra-thin injectable optoelectronics and sensors, Kim et al. and Koh et al. designed a process to pick up and transfer thin-film devices onto an epoxy-based needle and glue them together with silk-based solution, so that the needle is strong enough to bring the thin-film structure into the tissue and the film can detach soon after the silk glue or cellulose adhesive layer is dissolved.[52, 53] The precision of insertion is well maintained, whereas the surgical lesion/damage of the tissue is typically wider than 100 μm up to mm in size, possibly because the choice of materials of the supporting structure requires a larger geometry for enough rigidity, and the dissolvable layer is incompatible with lithographic process which

also limits the scaling down of the device size. Most recently, Luan et al. demonstrated an ultra-flexible nanoelectronic probe that can be implanted with surgical damage as small as 7 μm with the aid of an insertion shuttle made of tungsten wire or carbon fiber.[54] Nevertheless, such process requires an elaborated focus ion beam sharpening of each shuttle and an assembling procedure for each insertion.

2.2 Probe Design

All these pioneering and trending studies demonstrate the importance of matching the size and mechanical properties of the implanted functional devices with live cells and tissues, and the desire to minimize the impact of lesion while maintaining the feasibility of accurate surgery with rigidity. However, it is still a rather difficult task to reconcile the request for scaling down the size of probe, maintaining the mechanical strength required for accurate implantation surgery, while having the core functional structure small and flexible enough for better interfacing with cells. In addition, all existing implantable flexible devices require additional preparation of a carrier/support facility and/or manual assembly procedure, which increases the difficulty in scaled up production, and complicates practical uses. To address these existing challenges, here we report a general fabrication framework utilizing an inorganic biodegradable sacrificial layer that can be integrated in a unified top-down lithography procedure for preparing ultra-small probes, which can be used out-of-box, to accurately deliver ultra-flexible devices in deep tissue with minimal lesion by the *in situ* formation of the flexible functional structures only after the surgery process.

The schematics of the fabrication procedures and the probe structure are shown in Fig. 4. Specifically, there are three main fabrication stages. In stage (I), a double side polished (100) silicon substrate with 150 nm Si_3N_4 coating is first patterned with a biodegradable metal sacrificial layer (discussed in more details below), before a thin-film device structure is fabricated on the top using standard top-down lithographic procedures. The device layer features bonding areas which will be used for external connections, and a long arm of device(s) that fits into the final shape and dimensions of the probe. In stage (II), a reactive ion etching (RIE) process from the top side is used to carve out the probe body with a patterned photoresist layer as the mask, leaving a thin neck connection between the bonding area and the outer frame area. The depth of the RIE in this step defines the final thickness of the probe, typically in the range of 10-30 μm. In stage (III), the whole probe is shaped by a backside RIE process, which uniformly reduces the thickness of the whole substrate from the back until the area that has been thinned in the previous stage is completely removed and the probe body is isolated in full suspension. The resulting probe will have a thin neck connection to the supporting frame and can be easily detached by a notch. In summary, three layers are defined all by lithography in this process, including (1) the top device layer which typically has conductive metal connections passivated by insulating polymer shells, (2) the middle biodegradable sacrificial layer, and (3) the 10-30 μm thick rigid silicon beam which provides the mechanical strength with the smallest cross-section profile for the precise insertion surgery. Here for simplicity without losing generality, we use metal electrode pairs passivated by SU-8 polymer to demonstrate the feasibility of our proposed strategy and surgical procedures.

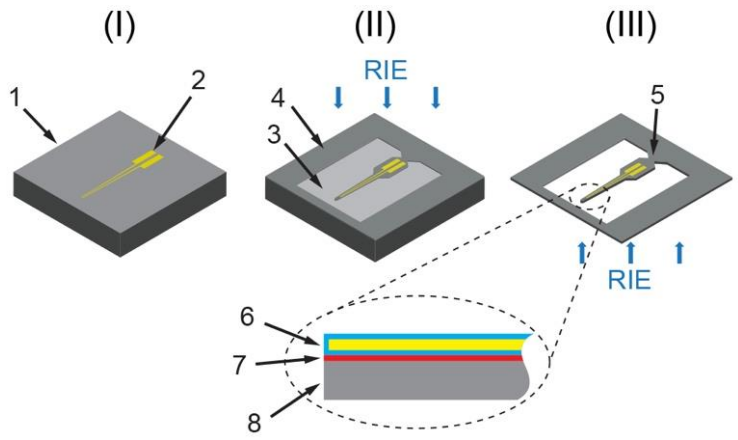

Figure 4. Schematics of fabrication procedures and probe structure. (I) On a 300 μm thick double-side polished (100) silicon substrate with 150 nm Si_3N_4 coating (1), the biodegradable sacrificial layer and thin-film device layer with bonding areas (2) are fabricated successively using standard top-down lithographic procedures. (II) The probe body is carved out by a top-side RIE process. During the RIE, a photoresist pattern is used as the etching mask to define and protect the probe profile as well as the outer frame area (4) while the opened area (3) is thinned down for 10-30 μm. (III) The silicon substrate is uniformly etched by a back-side RIE process until the thinned open area in stage (II) is completely removed, resulting in a fully isolated probe structure that has a narrow neck connection (5) to the outer supporting frame. Inset, cross-section of the probe structure. The thin-film device layer (6) and biodegradable metal sacrificial layer (7) are on top of a 10-30 μm thick silicon shaft (8). For clarity, the dimensions are not drawn to scale.

There are several key considerations of this design. First, we choose silicon to construct the initial supporting structure, which can be easily shaped for optimal surgical insertion by standard lithographic processes, and has a Young's modulus of ~165 GPa so that the critical dimension of the probe can be shrunk down to 10 μm level and still provide enough rigidity for implantation. Second, the biodegradable material for the sacrificial layer is chosen based on several criteria: (1) It must be compatible with top-

down lithography procedures so that the functional devices can be miniaturized and accurately aligned in a unified fabrication protocol for scalable production; (2) The dissolution of the material must only involve the physiological biofluids without the assistance from additional chemicals or enzymes; (3) The outcome of the dissolution of the material must not affect the physiological status and functionality of the neighboring cells. Third, the gradual dissolution of the sacrificial layer in physiological environment triggers the formation, separation and release of the flexible and functional devices from the rigid supporting beam, which happens all *in situ* within 15-30 minutes after the implantation such that the precise adjustment of the probe position can be performed after insertion without prolonged waiting or surgical complications. Last, these fabrication procedures can be generally used for preparing thin-film probes of arbitrary sizes and shapes for accurate implantation and the surgical procedures we demonstrate below can be adopted for either a single probe or for probe of arrays of device arms.

2.3 Biodegradable Material for Sacrificial Layer

There have been many reports on integrating biodegradable materials into implantable or surface-mounting electronic devices.[50, 55] Most widely studied materials used for packaging or gluing components are organic based, such as poly glycolic acid, poly L-lactic acid, and silk fibroin.[56-58] To date these materials are either not compatible with top-down lithography, or in the case of photo-crosslinkable silk protein, additional enzyme protease XIV is required to initiate a very slow degradation which is not practical for use with live cells *in vivo*.[59] In addition, carboxymethyl cellulose (CMC) or

polyethylene glycol (PEG) based dissolvable needles of hundreds of μm in diameters have been proposed to deliver thin film devices into tissue, but the size of the lesion is overall very large due to the weak mechanical strength and the expansion of probe volume after insertion during the dissolution process could potentially cause secondary damages.[60-62] On the other hand, inorganic biodegradable materials, including metals, such as Mg, AZ31 Mg alloy, Zn, Fe, W, Mo, and semiconductor and dielectric materials, such as Si, SiO_2 and MgO and ZnO, have been investigated for use as electrodes, connections, or surface coatings, but no study of using them as sacrificial layer has been reported.[63, 64] Here for the first time, we choose Mg to construct a biodegradable sacrificial layer, because it has a decent dissolution rates of 4.8±2.2μm/h in simulated body fluids, and the toxicity when fully digested within a short time can be tuned to be within tolerable limits.[64] The dissolution time, shelf life, and biocompatibility of Mg-based sacrificial layer is investigated as shown in Fig. 5.

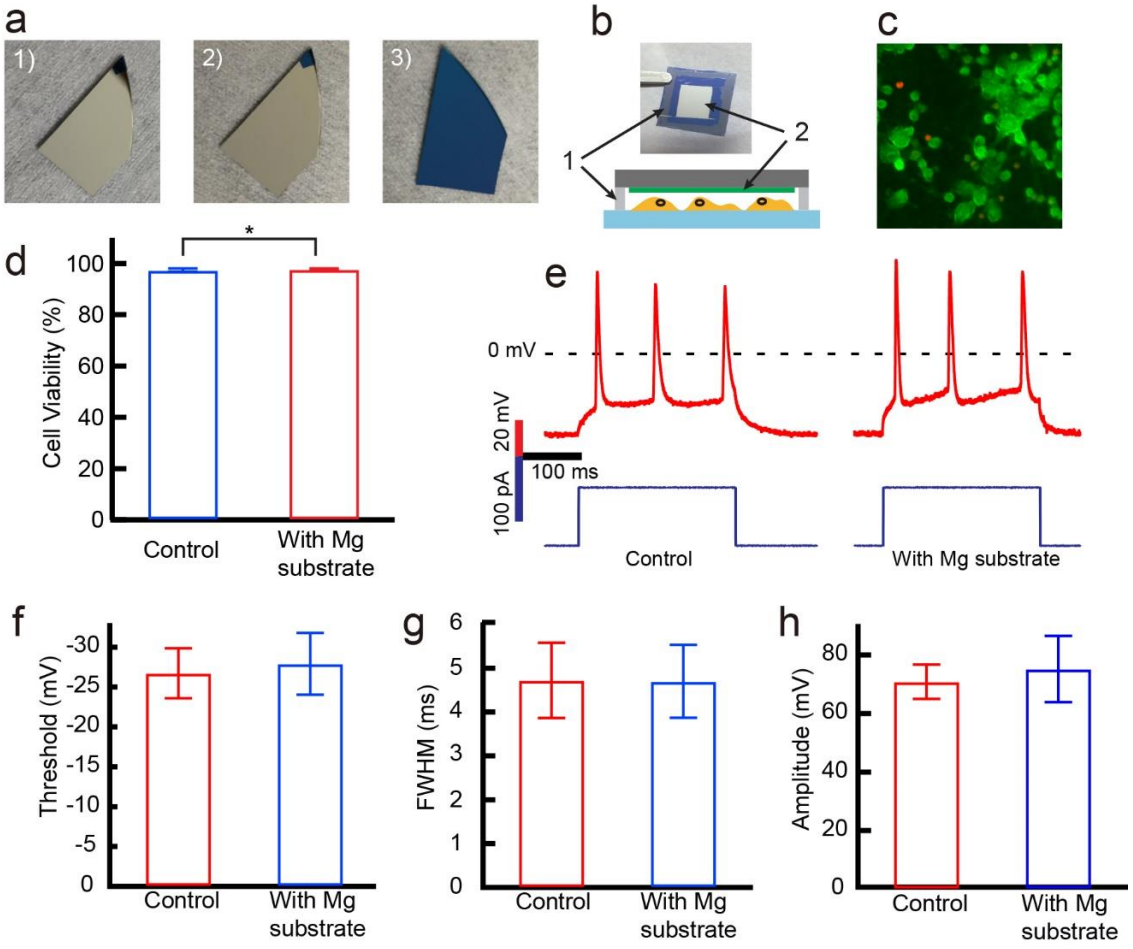

Figure 5. Characterization of Mg biodegradable sacrificial layer. (a) Shelf-life and dissolution time test. 1) A 100 nm Mg layer was thermally evaporated on a blank silicon substrate. 2) The freshly prepared sample was then stored in ambient environment (humidity <10%) for 10 weeks and the metal film did not show quality degradation. 3) After 10 week's storage, Mg layer can be dissolved in 1×PBS within 2 minutes. (b) Cell viability test setup. A 100 nm Mg layer (2) was deposited on a 15 × 15 mm silicon substrate where the edges were covered by 10 µm thick SU-frame spacer (1) mimicking the typical distance from a cell to the sacrificial layer on probe. This silicon substrate was flipped over and placed on a coverslip on which the 7 DIV rat cortical neurons were cultured. Scale bar, 5 mm. (c) Typical fluorescence microscope image of cells cultured with Mg-evaporated substrates for 20 hours. Green color represents live cells and red signals represent dead cells. (d) Cell viability of control group and cells cultured with Mg-evaporated substrates. The viability of cells cultured Mg-evaporated substrate was 97.7±0.3%. Control group viability is

97.3±0.6%, n=9, total number of cells analyzed=1280, *p=0.22. (e) Representative traces (red) of action potentials of the control group and Mg substrate co-cultured group. 5 cells from each group were patched in current-clamp mode (current traces are in blue). (f) The action potential threshold of control group (-27±3 mV) and cells cultured with Mg-substrate (-28±4 mV), p=0.61. (g) Full width at half maximum (FWHM) of control group (4.7±0.9 ms) and cells cultured with Mg- substrate (4.7±0.8 ms), p=0.96. (h) Spike potential amplitude of control group (71±6 mV) and cells cultured with Mg- substrate (75±11 mV), p=0.47.

Specifically, we have tested the dissolution time in 1× phosphate buffer solution (PBS) of a 100 nm Mg layer deposited on a blank substrate when it was freshly prepared, and after 10 weeks' storage in ambient environment (relative humidity controlled below 10%). In both cases, the Mg layer dissolved cleanly within 2 minutes (Fig. 5a), and did not show any degradation of its quality. When a top layer of thin-film devices is fabricated atop, the dissolution is limited to progress only from the sidewalls of the Mg layer. Therefore, the full undercut etching of the sacrificial layer and release of device structures of tens of millimeters in width and length is typically slowed down to take 15-30 minutes, and all probes have demonstrated > 6 months of shelf life in our tests. In addition, the impact on live cells from the dissolution of the Mg sacrificial layer is evaluated *in vitro* by a cell viability test. Rat cortical neuron cells (E18 Rat Cortical, Genlantis) were used for cell culture and viability test. Key steps in cell culture are as follows. First, NeuroPure tissue was digested using NeuroPapain Enzyme. The cells were suspended in NeuroPure Plating Medium (Genlantis) and cultured on round glass substrates (#1.5 thickness, 15 mm, Warner Instruments) in a 12-well cell culture plate at the initial cell density of ~1×105 cm^{-2}. The culture was maintained at 37 °C, 5% CO2

with the first full medium change in 24 hours, and following change of 50% medium every 2 days. As shown in Fig. 5b, a 100 nm Mg layer was deposited on a 15 mm × 15 mm control silicon substrate, where the edges of the substrate were covered by a 10 μm thick SU-8 frame spacer by photolithography. The SU-8 spacer simulates the typical thickness of an implanted probe and the spacing between the sacrificial layer and neighboring live cells, and helps to avoid direct mechanical damage to the cells in this test. The chip was then flipped over to make contact with neurons 7 days *in vitro* (DIV) cultured on a cover slip in a 12-well plate. After 20 hours culturing, cell staining was done using the LIVE/DEAD reduced biohazard viability kit (L-7013, Thermo Fisher Scientific). The viability test mechanism is based on the differential permeability of live and dead cells for two fluorescent dyes in this kit. A green fluorescent nucleic acid stain (SYTO 10) is membrane-permeable and labels all cells. A red fluorescent nucleic stain (DEAD Red) is cell-impermeant and labels only cells with broken membranes.[65]

To perform cell staining, the cell culture medium was first replaced by an equal volume of freshly prepared HEPES-buffered saline solution (135 mM NaCl, 5 mM KCl, 1 mM $MgSO_4$, 1.8 mM $CaCl_2$, 10 mM HEPES, pH 7.4). Then, the HBSS was replaced by 500μL of 1:1 mix of fluorescence dyes (1:500 diluted in HBSS). Cells were incubated with fluorescence dye solution in darkness for 15 minutes at room temperature. After staining, cells were fixed with 4% glutaraldehyde in HBSS. After 1-hour incubation with fixative, cells were washed with HBSS. The cell culture glass substrate was then mounted upside-down on a microscope coverslip for fluorescence microscopy. Microscopic images were captured by Nikon Eclipse Ti-U microscope with Texas-Red and EGFP filters. Fig. 5c shows a typical image of the fluorescence signals from the samples where

the red signals showed the dead cells and green signals showed the live cells. For cells cultured with the Mg coated substrates, the viability was 97.7±0.3%, which is statistically the same as the 97.3±0.6% of the control group (Fig. 5d). The local Mg^{2+} concentration increase is estimated as following: For simplicity, we use a 1D model where Mg is dissolved from an infinite plane and start diffusion in one direction. Given the diffusion coefficient of Mg^{2+} in solution as $7.05x10^{-6}$ cm^2/sec, within 10 minutes the diffusion distance of Mg^{2+} in free medium will be ~950 μm. Since inside the tissue the diffusion would be constrained by the surrounding cells, we can assume an order of magnitude smaller diffusion distance of ~ 100 μm which gives us the higher limit of the impact. For a Mg film of 100 nm, the average local concentration increase is about 0.04 mM. Since the extracellular Mg^{2+} concentration ranges from 2 mM for the brain to 1.2 mM for the heart,[66, 67] such concentration increase is less than 3.5% down to 2%. Since in real scenarios the diffusion would be a 3D model, the above numbers define the higher limit of concentration change. In addition, the increase of extracellular Mg^{2+} concentration generally will introduce suppression of neuron activities, or cardioprotective effects,[68, 69] The *in vitro* study of survival effects on hippocampal neurons of Mg^{2+} showed that >1mM increase of concentration would start to show trend of neuronal loss ($p=0.07$),[70] which is well above our estimated value. Therefore, we believe that the dissolution of Mg sacrificial layer would have minimal impact on neuron viability.

In addition, we investigated the excitability of neurons that have been co-cultured with Mg substrate with the same procedure in Fig. 5b. Specifically, Rat hippocampal neurons were co-cultured with a 15 mm × 15 mm silicon substrate which has a 100 nm

Mg layer and 10 μm thick SU-8 frame spacer for 6 days starting at 8 days *in vitro*. Whole-cell patch clamp recording was performed to examine the physiological properties of neurons. The patch pipette was pulled from a 1.5 mm diameter boron glass tube (Warner Instruments) on a P-1000 micropipette puller (Sutter Instruments). The pipette was filled with freshly prepared intracellular medium (in mM, Potassium gluconate 130, NaCl 10, HEPES 10, Mg-ATP 3, EGTA 1, Na-GTP 1, $CaCl_2$ 0.133, pH=7.3, osmolarity=290 mOsm), and the resistance was measured to be ~7 MΩ. Extracellular medium used was pH=7.4, osmolarity=300 mOsm solution containing 138 mM NaCl, 4 mM KCl, 2 mM $CaCl_2$, 1 mM $MgCl_2$, 0.33 mM Na_2HPO_4, 10 mM HEPES, 10 mM D-Glucose. In current-clamp mode, a +90 pA current pulse of 250 ms was injected to the neuron to initiate action potentials. The traces were recorded by HEKA EPC 800 and InstruTECH ITC18 (Harvard Bioscience, Inc) controlled by a customized program (script can be found on https://github.com/Qing-LAB/qinglab-IgorTools) run on Igor Pro (WaveMetrics Inc.). The action potentials were analyzed and compared following the method used by Dribben et al in their investigation on Mg^{2+} effect on neurons[70] as shown in Fig. 5e. The threshold (Fig. 5f), full width at half-maximum (FWHM) (Fig. 5g), and peak amplitude (Fig. 5h) of the action potentials did not show differences between the two groups. Therefore, the local Mg^{2+} concentration increase caused by the dissolution of the Mg sacrificial layer was not significant enough to change the neuron excitability.

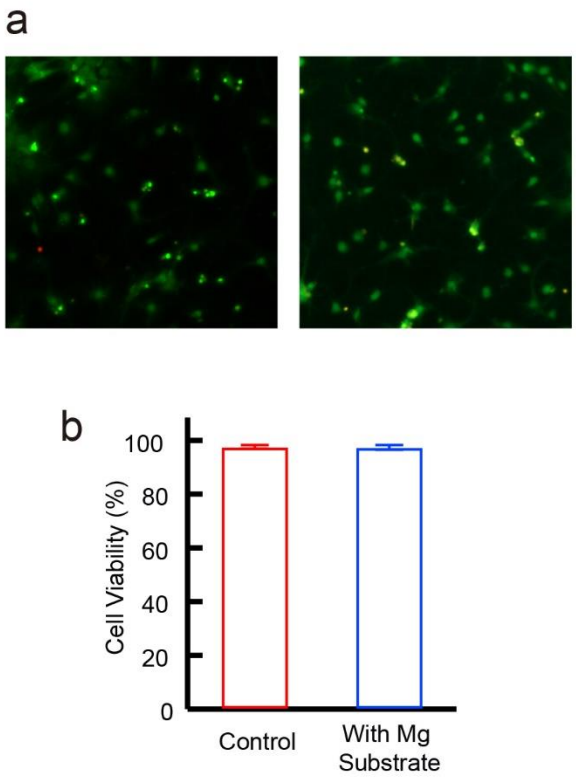

Figure 6. Mg dissolution effect on astrocytes viability. (a) Representative fluorescence images of control group (left) and Mg substrate co-cultured cells (right). (b) Cell viability of control group and cells cultured with Mg-evaporated substrates. The viability of Control group viability is 97.5±0.7%. The viability of cells cultured Mg-evaporated substrate was 97.4±0.8%. Total number of cells analyzed=876, p=0.75.

Last, we have also performed *in vitro* evaluation of the response from E18 rat astrocytes to the probes in terms of viability and immune response. To teste the effect of Mg dissolution on astrocytes viability, rat hippocampal astrocytes were co-cultured with Mg-substrate for 7 days before fluorescence staining. Cell staining was done using

LIVE/DEAD reduced biohazard viability kit (L-7013, Thermo Fisher Scientific), the same dye as what has been used in cortical neuron viability test. Cells were incubated with fluorescence dye solution in darkness for 15 minutes at room temperature. After staining, cells were fixed with 4% glutaraldehyde in HBSS. After 1-hour incubation with fixative, cells were washed with HBSS. The cell culture glass substrate was then mounted and sealed on another microscope coverslip for fluorescence imaging on a Nikon Eclipse Ti-U microscope with Texas-Red and mCherry filters. The viability for astrocytes co-cultured with Mg-evaporated substrate was 97.4±0.8% vs 97.5±0.7% in the control group (p= 0.75) (see Fig. 6).

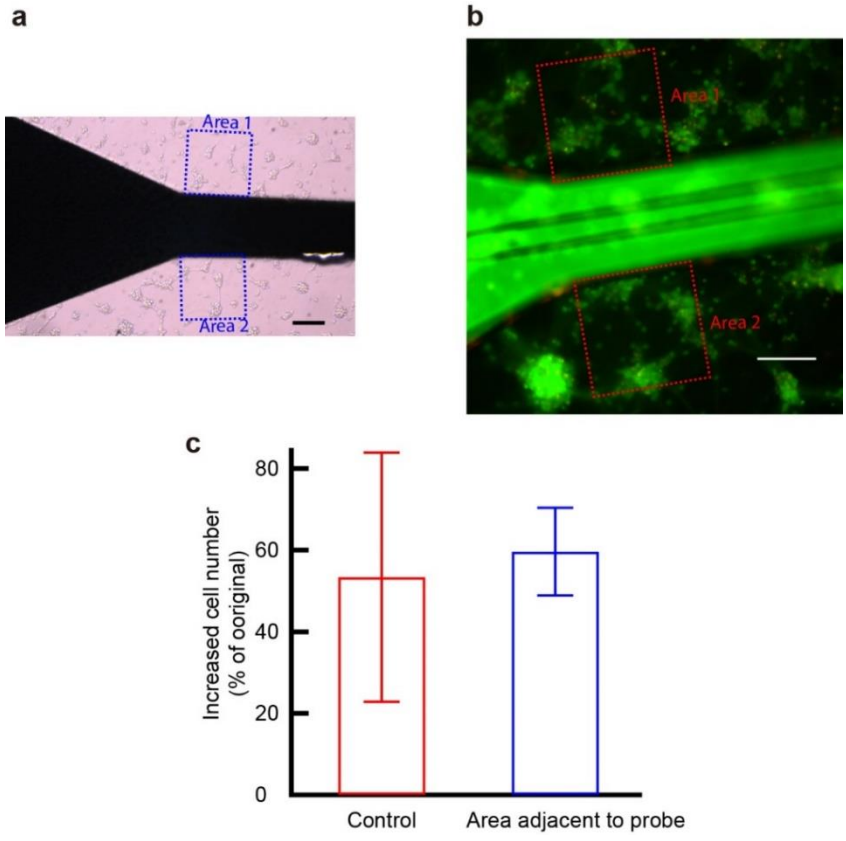

Figure 7. *In vitro* test of astrocytes response to co-cultured probe. (a) Typical microscope image of cells at day 3. Scale bar, 100 µm. (b) Typical fluorescence image of the same group of cells at day 14. Scale bar, 100

μm. (b) Proliferation rate of control group and cells adjacent to probe. The proliferation rate of cells within 200 μm from the probe edge was 60 ± 10%. The proliferation rate of control group was 53 ± 30%. Total number of areas analyzed=6, p=0.76.

Since immune response leads to significantly higher astrocytes proliferation,[71,72] the astrocytes proliferation rate can be used as an indicator of immune response to probe. The procedures of astrocytes proliferation rate evaluation are as follows. Rat cortical astrocytes were plated on round glass cover slip (diameter=15 mm). Images of astrocytes were captured by Nikon Eclipse Ts2R microscope on day 3 to capture the density of cells. Then a type-II probe was placed on the cover slip, fixed by a small drop of silicone glue (Kwik-Sil adhesive, World Precise Instruments) applied at one end. The astrocytes were co-cultured for 2 weeks before staining. Same dye and staining method were used as described before. Images were taken on a Nikon Eclipse Ti-U microscope with Texas-Red and mCherry filters. According to statistical results, the proliferation rates of astrocytes within 200 μm from the edge of the probe was 60 ± 10% vs 53 ± 30% in the control group (p=0.76) (Fig. 7). Compare to reported astrocytes enrichment up to 100-300 μm from the surface of implanted electrode 2 weeks postinjection,[71] our probe design does not seem to induce significant astrocytes immune response. In summary, our preliminary *in vitro* data suggest that our biodegradable sacrificial layer would not negatively impact the physiological status of neurons cells. Nevertheless, *in vivo* immune histochemical study of the tissue response to the dissolution of the Mg sacrificial layer will be necessary to fully evaluate the biocompatibility of our design and will be performed in a follow-up study.

2.4 Fabrication and Assembly of Type-I Probe

Based on the proposed fabrication procedures, here we demonstrate two types of designs of probes for different applications. In type-I probes, a 3D bend-up structure is spontaneously formed on the thin silicon supporting shaft shortly after the probe is exposed to physiological fluids due to the integrated stress within the thin film structure. In type-II probes, the whole ultra-thin device layer is accurately released with all rigid structure completely removed soon after surgery.

Fig. 8a shows the schematics of the basic structure of type-I probe. The Mg sacrificial layer was defined locally (red area in Fig. 8a) below the end terminals of the thin-film device, and the rest of the top layer was directly anchored on the silicon supporting shaft. The part of the device arms on top of the Mg layer was composed of Cr/Pd/Cr (1.5 nm/75 nm/50 nm). When the Mg layer is dissolved in physiological solution, this free ending of the device will turn from the planar structure into a 3D bend-up structure due to the built-in stress, similar to the bend-up structure utilizing Ni as sacrificial layers as reported previously.[38] The deflection of the dual-metal film is proportional to the product of the average intrinsic stress and the film thickness. In order to obtain the required geometry, tensile stress in metal film is required. In addition, the two layers of metals should have comparable stress-thickness product to generate similar deflection to avoid deformation or separation of the two films. We used 75 nm Pd and 50 nm Cr as optimal combination for our bend-up structure, which have tensile intrinsic stress, and provide 4.4×10^{-4} dynes/cm and 4.9×10^{-4} dynes/cm respectively.[73] This

design would allow us to insert the probe into the tissue, and the functional thin-film device will be able to spontaneously form a 3D structure that deviates away from the lesion caused by the surgery so that only the flexible part of the device will get in contact with the active cells in the surrounding space (Fig. 8a right).

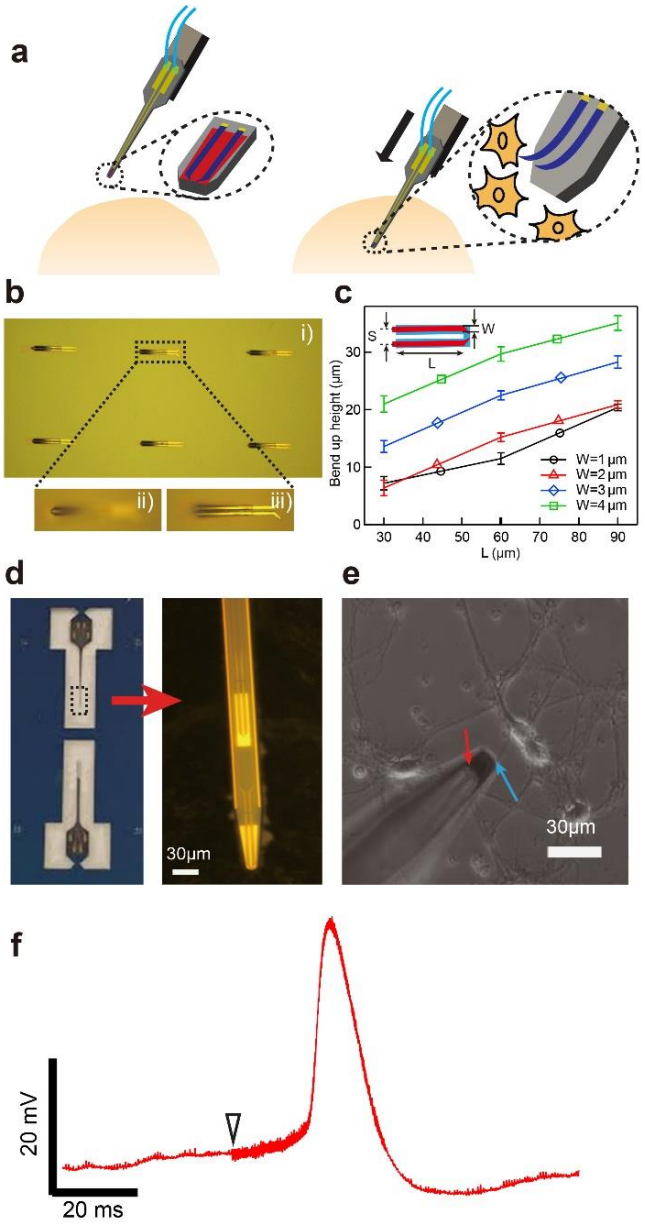

Figure 8. Probe with 3D flexible thin-film bend-up structure. (a) Schematics of probe implantation and *in situ* formation of bend-up structure. Left: The backside of silicon shaft is glued to a probe holder of micro-

manipulator (brown). The bonding area is connected to external instrumentation by silver paste (green) and conductive wires (blue). Zoom (dashed black circle) of basic structures at probe tip showing the thin-film flexible structure (blue) is held by Mg biodegradable sacrificial layer (red) before implantation. Right: *In situ* formation of 3D flexible thin-film bend-up structure. The black arrow indicates the insertion direction. Zoom (dashed black circle) of thin-film device shows the functional thin-film device spontaneously forms a 3D bend-up structure after implantation. (b) Bright-field optical microscope images of bend-up structures. i) Array of bend-up electrodes in 1×PBS. ii, iii) Close-up view of a thin-film bend-up electrode structure. Microscope was focused on ii) electrode tip and iii) anchor part of a same electrode structure, respectively. Images were taken using a water-immerse lens. (c) Bend-up height of the thin-film structure as a function of electrode dimensions. The bend-up height increased with electrode length and width. The measurement was done in PBS solution for metal layer composed of Cr/Pd/Cr (1.5 nm/75 nm/50 nm). Inset, top-down schematics of electrodes (red) geometry in thin-film structures. L, W, and S represent the electrode length, width, and distance between electrode pair. (d) Left: Camera image of probes connected to a supporting frame with a thin neck structure. Right: Zoom-in view of electrode site at probe tip. Image was taken by bright-field optical microscope. Scale bar, 30 μm. (e) Microscope image of *in situ* formation of 3D thin-film bend-up structure in neuron cell culture medium. Electrodes tip deviated from its original position (indicated by blue arrow) to form a 3D structure of which the apex is indicated by the red arrow. Scale bar, 30 μm. (f) Action potential recorded from a cell stimulated by a type I probe. Signals were recorded by patch-clamp pipette from the same cell. The triangle marks the time when a 0.5 V, 50kHz pulse was applied.

The fabrication procedures of Type-I probe are illustrated by Fig. 9. The fabrication started with the construction of electrodes and sacrificial layer on top side of a 300 μm thick silicon substrate with silicon nitride coating (150 nm Si_3N_4/100nm thermal SiO_2 on 300 μm n-Si, double side polished, University Wafers) by standard lithography techniques (Fig. 9a). Specifically, metal connections and bonding areas (Au/Cr, 55/2 nm)

were first patterned on the silicon substrate by standard photolithography, metallization and lift-off processes. Next, the sacrificial layer pattern was lithographically defined where the 3D electrodes would be located. A 100 nm Mg layer was deposited by thermal evaporator (Cressington 308R) and lift-off by Remover PG (MicroChem). To construct the 3D electrodes, firstly a layer of 0.5 μm thick SU-8 polymer (SU-8 2000.5, MicroChem) was shaped by photolithography on top of the sacrificial layer, serving as the bottom passivation layer of 3D electrodes. Next, electrode pairs with internal stress (Cr/Pd/Cr, 1.5/75/50 nm) were fabricated on the bottom passivation layer, followed by another layer of 0.5 μm SU-8 polymer as the top passivation (Fig. 9b). The final shape of the rigid probe structure for implantation was defined in the end by Reactive Ion Etching (RIE). Specifically, a 3-μm-thick photoresist mask (S1818, MicroChem) was patterned on top side of the silicon substrate by photolithography which defined the shape of a probe. The top surface of the silicon substrate was then etched by RIE (STS ICP Advanced Silicon Etching, Fluorine) for 10-30 μm. During the etching process, the photoresist mask protected the probe structure as well as the supporting frame while only the open areas were etched, forming a 10-30 μm thick plateau of the shape of the final probe with one thin neck connection to the supporting frame (Fig. 9c). Last, the silicon substrate was etched uniformly from the back side by the same RIE process until the open windows on the front side was completely removed, resulting in a 10-30 μm thick probe (Fig. 9d).

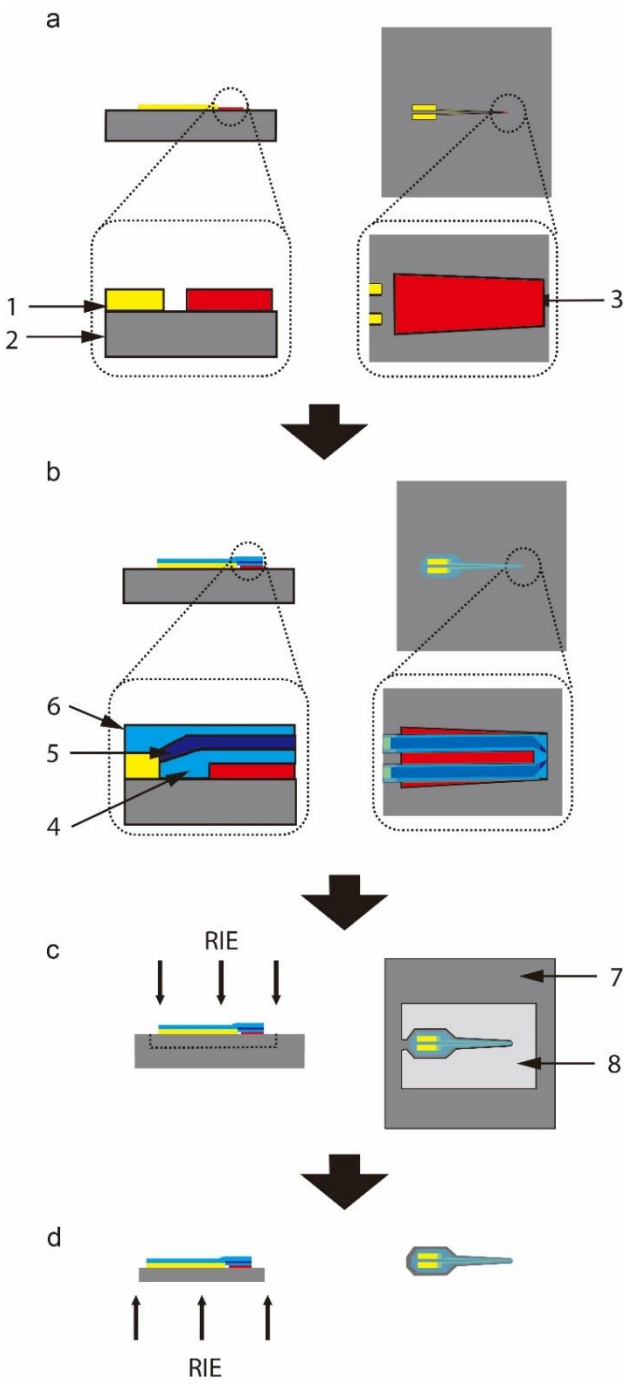

Figure 9. Top-view (left) and cross-section (right) of fabrication procedures of type I probe. a) The sacrificial layer (3) and gold bonding areas and connections (1) were fabricated on the top side of a 300 µm thick double polished silicon substrate (2). b) Fabrication of the thin-film device layer. The device layer consists of a bottom SU-8 (4), Cr/Pd/Cr electrodes (5), and a top SU-8 layer (6). c) Top side RIE etching

process. Open areas (8) were etched for 10-30 μm while the photoresist pattern protected area (7) stay intact. d) Back side RIE etching process. A probe was fully isolated after the etching process and breaking the narrow neck connection. For clarity, the dimensions are not drawn to scale.

Arrays of locally bend-up structures on a planar silicon substrate have been fabricated to test the dissolution time and the yield of the formation of the bend-up structure in PBS solution. All samples have shown consistent dissolution time within 20 minutes and yield >93% (Fig. 8b), independent of the shelf life of the samples (ranges from a couple of weeks up to six months).

In order to have the functional devices of type-I probe positioned in tissue properly, the bend-up height and the bend-up moment need to be tuned such that the devices can be positioned closer to the active cells with optimal stiffness. This can be achieved by adjusting the dimensions of the electrodes. Specifically, we kept the distance between the electrode pair fixed as S = 8 μm for a small cross-section profile, and observed that the bend-up height increased with the length L of the electrodes for different electrode width W (Fig. 8c). This can be understood by the same model used in previous reports: The total bend-up stiffness per unit width D of the structure, can be calculated as: $D = \alpha_s \cdot D_s + \alpha_m \cdot D_m$, where α_s and α_m are the area fraction of the SU-8 polymer and metal part, D_s and D_m are the bending stiffness per unit width of polymer and metal part, respectively.[74] In our design, $\alpha_m = W/(W+2)$, where W is the width of metal electrodes. Since D can also be expressed as $D = M/(c \cdot d)$, where M is the bending moment, d is the total width, and c is the curvature of the bending, we have: (1) When

bending against the same load, such as in our tests in free medium, the curvature would remain constant, and bend-up height h increased with the length of the electrodes; (2) As the width of the metal electrodes increased, α_m and D_m increased accordingly, which led to increased curvature and thus higher bend-up height under the same load and electrode length; (3) For the same electrode length and bend-up height, increasing the width of the metal electrodes would lead to higher bending moment, which means that the structure would be able to penetrate into tougher tissue structures. In addition, from Fig. 8c, we can see that for the same length of the electrodes, the bend-up height increased significantly only when W was above 2 μm. For W = 2 μm, the bend-up height followed pretty close to the case when W = 1 μm. This can be attributed to the larger contribution of $\alpha_s \cdot D_s$ when α_m is small.

A photo of an as-fabricated probe is shown in Fig. 8d, in which multiple local bend-up structures have been defined along the length of the probe body. Such probes have been tested *in vitro* to interface with individual neurons, as shown in Fig. 8e. The probe was mounted on a micromanipulator with an angle of 25~30 degrees and the thin-film electrode pairs facing down. After inserting the probe into neuron recording medium, the Mg sacrificial layer was completely dissolved within 15 minutes, and the thin-film electrodes bended downward by ~20 μm. The ends of the electrodes were originally aligned with the tip edge of the probe before the bend up and in the image it was clearly retracted as a result of the bend-up and the projection of the imaging angle. The device can be used to target and contact individual neurons for localized stimulation. In order to stimulate cultured cells, the backside of a type-I probe was glued (Devcon 5-

minute epoxy, ITW) to a printed circuit board (PCB). The bonding pad areas on the probe were electrically-connected using silver epoxy (Epoxy tech, EJ2189), cured at 80 °C for 3 hours and subsequently passivated by silicon elastomer (Kwik-Sil adhesive, World Precise Instruments). Then, the PCB was screw-mounted on a motorized micromanipulator (MPC-385, Sutter Instruments). The probe can be manipulated in three dimensions to target specific cells and electrically stimulate the cell and a patch pipette, which is also mounted on a manipulator, was used to record the action potential stimulation of the same cell. The patch pipette was pulled from a 1.5 mm diameter boron glass tube (P-1000 micropipette puller, Sutter Instruments). The pipette was filled with freshly prepared intracellular medium (in mM, Potassium gluconate 130, NaCl 10, HEPES 10, Mg-ATP 3, EGTA 1, Na-GTP 1, CaCl2 0.133, pH=7.3, osmolarity=290 mOsm). After a giga-seal was formed, the pipette was held at -70 mV and then the cytomembrane was broken to form a whole-cell patch. Afterwards, the voltage was changed to -40 mV, followed by applying 0.5 V, 50 kHz pulse using the probe to stimulate the cell, thus action potentials are generated (see Fig. 8f). The limit for such *in vitro* use of the probe is that the access angle of the probe must be kept shallow as the rigid tip of the silicon shaft will interfere with the contact when the angle is too steep.

2.5 Fabrication and Assembly of Type-II Probe

In addition, type-II probes are designed to accurately implant fully flexible devices without any rigid structure remaining in the tissue at all. As shown in Fig. 10a, type-II probes have all the functional connections and devices integrated within the top

thin film structure, which is fabricated on the Mg sacrificial layer covering the entire surface of the rigid silicon shaft. The as-prepared whole probe is rigid and robust enough so that it is easy to bond reliably with external wire connections directly, and to mount on a micromanipulator. After inserting the probe to the tissue, the whole top film structure is released from the silicon shaft, typically within 30 minutes, and the rigid shaft can be retracted following the exact same path of insertion from the tissue, leaving only the thin film staying with its shape and position unaltered. Here for the first time, we demonstrate high level of fidelity of keeping the shape and position of the thin-film probe when the thickness was as low as 2 μm, with the rigid shaft structure itself as thin as 10 μm, both of which are much smaller than previously reported results. Fig. 10b-10e show the whole process of implanting the thin-film probe into a tissue-mimicking agarose gel (1 wt.%, Young's modulus 40kPa), demonstrating (1) the as-prepared whole probe mounted on a micromanipulator holder with wire connections before insertion, (2) the whole probe inserted inside the gel, (3) release of the top thin film structure and retraction of the rigid silicon shaft after 30 minutes, and (4) full retraction of silicon shaft with the thin film probe remaining in the gel.

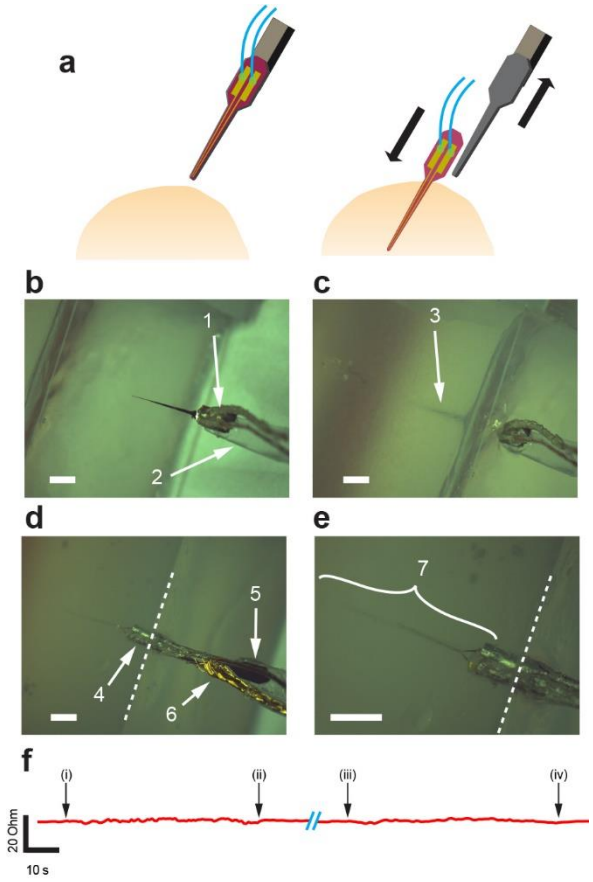

Figure 10. Ultra-flexible probe implantation. (a) Schematics of ultra-flexible probe assembly and implantation procedures. Left: Silicon shaft (grey) of the probe is glued to probe holder of a micro-manipulator (brown). Bonding area on the thin-film device side is connected to external instrumentation by silver paste (green) and conductive wires (blue). Right: The thin-film probe (magenta) fully delaminates from the silicon shaft typically in 30 minutes after insertion into tissue. The shaft can be fully retracted from the tissue leaving the position and the shape of device intact. (b-e) Stereomicroscope images show the whole process of implanting probe into 1% agarose gel mimicking brain tissue environment and detachment of the thin-film probe. (b) The bonding areas on thin-film probe (1) were connected to recording instruments and the silicon shaft was glued to probe holder of micro-manipulator (2). Scale bar, 2 mm. (c) The probe (3) was inserted into tissue-mimicking gel. Scale bar, 2mm. (d) 30 minutes after insertion, sacrificial layer dissolved. The thin-film probe (4) was fully released from the silicon shaft (5) which is then fully retracted from the gel, leaving only the thin-film probe (4) and the connected wires (6) in the gel. Scale bar, 2 mm. (e) The thin-film probe (7) in the gel. Scale bar, 2 mm. (f) Resistance recorded

from electrode pair which are shorted at the tip in the thin-film layer during insertion and thin-film detachment procedures. (i) marks the time when the probe enters gel. (ii) represents the time when the probe is completely inserted in the gel. (iii) and (iv) mark the beginning of pulling silicon shaft and the fully extraction of silicon shaft, respectively.

In addition, to track the integrity of the film structure and the functional device, we have used electron-beam lithography (EBL) to connect the metal electrode pairs at the very end with a thin gold film of dimensions 2 μm width × 2 μm long × 50 nm thick so that the resistance through the whole length of the electrodes can be tracked during the whole operation. The silicon backbone of the probe was glued onto a home-made polycarbonate probe holder. The electrical connection between the bonding area and the conductive wires (Cooner Wires, CZ1215-2F) was made by silver epoxy using the same technique described before. The connective wires were connected to Keithley 2636B Source Meter SMU instrument. All metal connections on the probe were passivated using silicon elastomer. The calculated resistance based on geometry of the electrodes was ~1430 ohm, and the measured result before the operation was 1390 ohm (Fig. 10b, 10f (i)), consistent with the estimation. Then the probe holder was assembled onto a single-axis translator (Thorlab, T12X) which had been mounted on a micro-manipulator XYZ stage (Thorlab, MBT616D). A 0.2 mV voltage was applied to the electrode pair by Keithley SMU to measure the conductance and the resulting current was recorded by the same instrument. The probe was precisely controlled by the manipulator to be inserted into target spot of the gel. As the probe entered the gel, we observe no distortion of the shape or the direction (Fig. 10c) which showed that the rigidity of the 10 μm thick silicon

shaft was enough to deliver the full structure into tissues with similar Young's modulus to the gel used here. The resistance between the electrode pair was constant during this process (Fig. 10f (ii)). After 30 minutes, the silicon shaft was gently retracted fully from the gel following the same path, while the thin film probe was left inside the gel (Fig. 10d, 10f(iii)). As the silicon shaft was fully retracted, the position and shape of the 2 μm thin film probe showed no distortion in shape nor size, with a consistently constant resistance reading (Fig. 10e, 10f(iv)). It is important to note that the gold bridge we defined by EBL was only supported by a 500 nm SU-8 layer on the bottom and therefore in our test, the thinnest part of the probe was only 550 nm. The < 1% change in the resistance of the test probe throughout the whole process proves the robustness of our design and protocol for implantation surgeries.

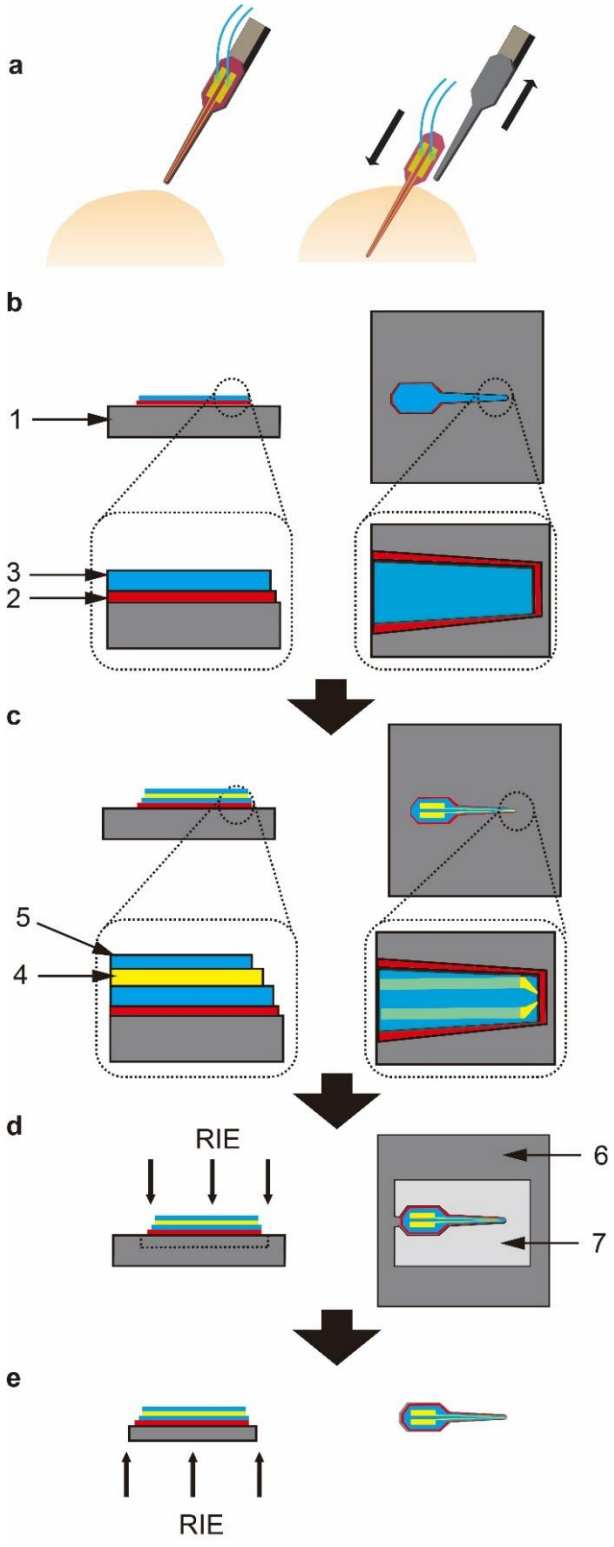

Figure 11. Top-view (left) and cross-section (right) schematics of type II probe fabrication procedures. a) Fabrication of sacrificial layer (2) and SU-8 probe layer (3) on silicon substrate (1). b) Fabrication of gold

electrodes (4) and SU-8 top passivation (5). c) Top side RIE etching process. Open areas (7) were etched for 10-30 μm while the photoresist protected area (6) stay intact. d) Back side RIE etching process. For clarity, the dimensions are not drawn to scale.

The fabrication of type II probe was based on a Si_3N_4 coated silicon substrate (150 nm Si_3N_4/100nm thermal SiO_2 on 300 μm n-Si, double side polished, University Wafers). A sacrificial layer (100 nm Mg by thermal evaporation) was first patterned on the top side of the silicon substrate by standard lithography techniques. To construct the fully flexible probe structure, a 2 μm thick SU-8 polymer (SU-8 2002, MicroChem) of the same shape of the final probe was lithography defined on top of the sacrificial layer, serving as bottom passivation layer (Fig. 11a). Next, electrode pairs, metal connections, and bonding pads (Au/Cr, 50 nm/2 nm) were fabricated on top of the 3 μm SU-8 layer, followed by another layer of 0.5μm SU-8 polymer (SU-8 2000.5, MicroChem) as the top passivation (Fig. 11b). The etching processes that defined final thickness and shape of the rigid probe structure were the same as described in the type I probe section, except that the resulting probe has the whole thin-film device structure on top of a continuous layer of sacrificial layer (Fig. 11c, d).

2.6 Conclusions

In summary, we have reported a fabrication framework and surgery procedures to prepare flexible ultra-thin-film devices that can be delivered accurately into tissue-mimicking gel samples with biodegradable sacrificial layer which allows (1) *in situ*

formation of 3D bend-up structures after the surgery, and (2) full release of the whole thin-film probe within the sample and the whole rigid structure completely removed afterwards. We have systematically studied the behavior of the bend-up structure with Mg sacrificial layers in biological fluids, and demonstrated that film probes as thin as 2 μm can be delivered accurately with intact geometry inside tissue and the lesion caused by the retractable rigid delivery structure can be as thin as 10 μm using our techniques. The *in vivo* biocompatibility of our probes remains to be verified in a follow-up study but *in vitro* test results and the estimated <0.04 mM increase in local Mg^{2+} concentration suggest that our design could provide a general out-of-the-box solution for accurately implanting ultra-thin and flexible device arrays that is compatible with scalable top-down production.

2.7 Future work

Based on this work, further investigations into flexible implantable bio-probes could be done in various areas. Firstly, the *in vivo* protocols for probe implantation and recording from anesthetized animals will be established. As stated in the introduction, chronic implantation in animal or human neural system is the main purpose of the bio-probes. Since fabrication protocol for probes have already be developed, surgical experiments need to be conducted to demonstrate the probe can work as communication bridge between neural system and artificial devices that features minimal invasion, implantation accuracy, and chronic implantation stability. To achieve this goal, future

experimental investigations are needed to establish optimal surgical procedures and signal recording.

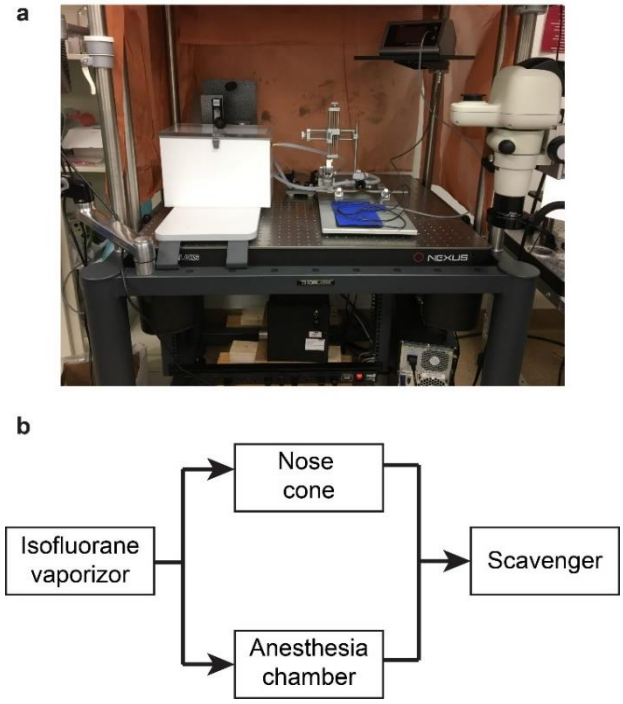

Figure 12. Anesthesia station. (a) Camera image of the anesthesia station setup. (b) Schematics of the isoflurane gas flow.

To date, an anesthesia system has been built. It consists of a vaporizer, an anesthesia chamber, a stereotaxic surgery platform, and a gas scavenger. Isoflurane and oxygen mixture, which serves as the anesthesia gas, is evaporated by the vaporizer and then flows to the anesthesia chamber and stereotaxic surgery platform. The anesthesia chamber is a sealed box with gas inlet and outlet. Live rats will be kept in this chamber for light anesthesia before surgery. During surgery, the rat will be fixed on the stereotaxic frame by a pair of metal bars. A nose cone with anesthesia gas inlet and outlet is covered on the rat nose to let it stay anesthetized. In case of survival surgery, a feedback-

controlled system, which includes a warming pad and a temperature probe, is used to maintain the rat body temperature at 37 ℃. Exhaust from both the anesthesia chamber and nose cone outlet will be collected and filtered by the scavenger. In the future, the surgical procedures will be optimized in rat cadavers first to determine the details of surgical parameters. Then the non-survival surgeries will be performed to optimize details of the process and placement of the probe. Then the non-survival surgeries will be performed to optimize details of the process and placement of the probe. The rats will first be anesthetized before cranial surgery to open a 2mm diameter hole in the primary somatosensory cortex region. Throughout the procedure, depth of anesthesia is checked by monitoring of tail pinch response, whisking, breathing rate, and eye and toe reflexes. If anesthesia is too light, the percentage of isoflurane will be slightly increased. The probe will be used for *in vivo* recording under anesthesia. The animal will then be euthanized after the recording. Ultimately, a survival surgery and chronic recording in vivo will be developed. Therefore based on the previous results, survival surgery will be performed and procedures will be developed for working with awaking animals to evaluate the long-term (4 weeks) *in vivo* recording performance of the bioprobes. The recording experiment will be conducted weekly under anesthesia after the rats recover from the surgery. With the 10 × smaller size and better mechanical matching with active neuron cells, it is expected to observe greatly enhanced biocompatibility and life-time.

Furthermore, the prospect of being able to wirelessly deliver signals after implantation serves as a continuous incentive for future research. The probe designs demonstrated in this work require wires for connecting external measurement devices. Such configuration brings complexity in bonding and makes it difficult to acquire signal

during chronic implantation. On the other hand, wireless data transmission is a desired feature since it allows real-time data acquisition without regulator and reduces labor in connecting wires to metal contacts pads on the probe. This goal can be achieved based on probes presented in this work. For example, combining antenna and implantable probes enables a wireless neural implant that can transmit data such as neuropotential wirelessly. As demonstrated in Fig. 13, a wireless antenna module consists of a polydimethylsiloxane (PDMS) bulk and gold antenna/interconnects is bonded to contact pads of the probe. This wireless microsystem, which is a variation on the recorder antenna reported by Chae *et al*., utilizes a fully passive scheme so that the system is powered by external sources through electromagnetic radiation.[75-78] Therefore, no internal battery is necessary, and the system size is further reduced. In addition, the curvy buffer connections can eliminate the tension and potential chronic irritation and damage to the surrounding cells associated with external wiring and micro-motions or vibrations. The existing probe fabrication processes can be easily adapted for the proposed new probe design. The silicon shaft will need to be enlarged to make enough space the PDMS antenna bulk. The as-fabricated antenna module will be bonded to the metal pads on polymer probe by silver paste or conductive ink. To implant the probe and antenna, the silicon back bone will be glued onto a micromanipulator holder. Then the probe will be inserted into desired position, while the PDMS bulk is remained outside of the skull. After Mg sacrificial layer dissolution and retraction of silicon shaft, signal recording tests will be performed to verify the system works properly. In case of successful data acquisition, the antenna PDMS bulk will be secured on the skull using dental acrylic. The wound will be sewed shut with sutures at its extreme ends. The improved probe design

discussed above is expected to have enhanced biocompatibility due to less micro motions, and stable chronic recording signals.

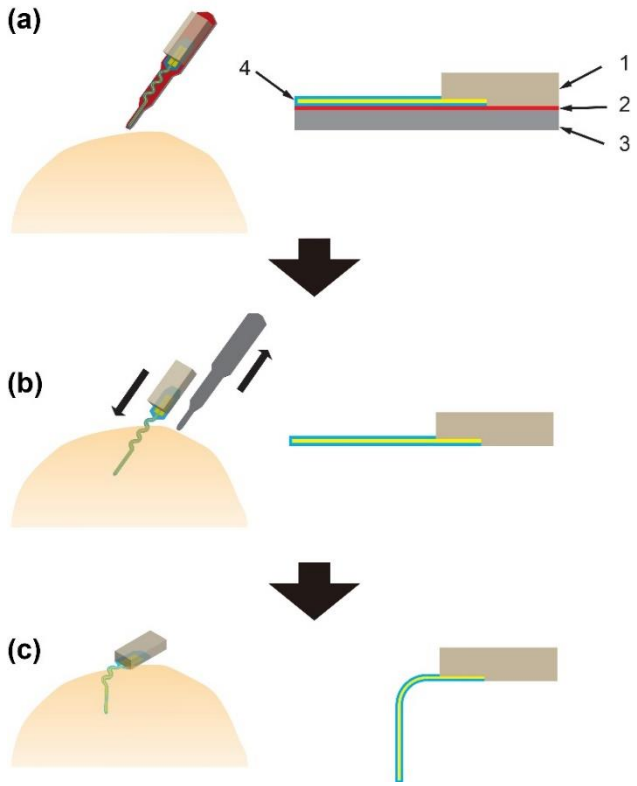

Figure 13. Schematics of ultra-flexible probe with antenna assembly and implantation procedures. (a) Left: The probe assembly consists of an antenna module (light brown), thin-film device layer (blue and gold), Mg sacrificial layer (red), and silicon shaft (grey). Right: Cross-section of probe assembly. The antenna module (1) is bonded to thin-film device layer (4). The thin-film device layer (4) and biodegradable metal sacrificial layer (2) are on top of a 10-30 μm thick silicon shaft (3). For clarity, the dimensions are not drawn to scale. (b) Left: The thin-film probe (blue and gold) fully delaminates from the silicon shaft after insertion into tissue. The shaft can be fully retracted from the tissue leaving the position and the shape of device intact. Antenna module remains outside of brain/skull. Right: Mg layer completely dissolves. Antenna bulk and thin-film probe detach from silicon shaft. (c) Left: After signal test, the antenna module

is secured on the skull using dental acrylic. Right: The thin-film probe is implanted in tissue. Curvy buffer connection and wireless data transmission reduces stress due to external wire fixation and micro-motions/vibrations after the implantation.

Further investigations into integrating nanomaterial-enabled device on ultra-flexible probe can be conducted based on this work. For example, replacing metal electrode pair with silicon nanowire will improve the probe functionality. Silicon nanowire is a proved outstanding material for bio-markers detection and extracellular recording.[79,80] Compared to passive metal electrodes, active nanowire sensors have higher spatial and temporal resolution, improved sensitivity, and stronger interaction with cells.[81] A single nanowire can be assembled on the electrode tip to form a highly sensitive field effect transistor biosensor by way of dielectrophoresis.[82] When nanowire suspension solution flows above the electrode pair, it is under the dep force. By tuning the voltage applied, a balance of the electric field force, dep, and force can be achieved. Therefore the nanowire hover above the electrode pair. Then, as flow is stopped/under certain conditions, the nanowire is assembled on the electrode pair, forming a nanowire sensor. In the presented probe design, the nanowire sensor can be on the tip of electrode or, in case of multiplexed recording, at multiple sites along the probe. The nanowires assembly is accomplished after electrodes fabrication and before front side RIE process. First, the Mg sacrificial layer needs to be protected by an extra masking process to avoid Mg sacrificial layer being etched by aqueous suspension solution. The sample surface is coated with polymethyl methacrylate (PMMA) and open windows for nanowire assembly are then defined by EBL exposure and development. Then a flow cell for nanowire deposition is built using similar method as reported by Freer *et al*. Nanowires assemble at

desired electrode sites driven by field forces. Finally, the PMMA mask will be removed by acetone, followed by consequent etching processes.

In addition, this study focuses on the material and structure designs and surgical strategy for implantable devices. Therefore, for simplicity and clarity, only single-channel probes were fabricated. However, multiplexing of devices is an often-desired feature, and additional follow-up study will be needed to find an optimal solution for the reported probe designs. For example, for Type-I probe, since the rigid structure of the Si backbone will remain after surgery, commercial wire-bonding and sealing method can be directly applied. Whereas for Type-II probe, a more delicate high-resolution process is needed. The conductive ink printing methods explored by Hong *et al*. [49] could be a potential solution.

3. CARRIER SPIN INJECTION AND TRANSPORT IN DIAMOND

3.1 Background

3.1.1 Introduction to Spintronics

Spintronics has attracted extensive attention as it uses spin-related phenomena, such as spin relaxation and spin transport, instead of using electron charge in conventional semiconductor physics.[83] It offers unique opportunities for development of next-generation electronic devices. For example, spintronics is a proven successful platform for novel data storage, featuring nonvolatility, lower power consumption, higher density and higher data processing speed. In addition, spintronics has shown great potential for quantum computing applications.

The Nobel-prize-winning discovery of giant magnetoresistive effect (GMR) in 1980s is one of the most important pioneer researches in spintronics. GMR refers to the phenomenon that the resistance of ferromagnetic layers changes with their relative magnetic orientations. It has already achieved commercial success in industry as hard disk read-head, magnetic sensor, and magnetoresistive random access memory (MRAM). A typical GMR device consists of two ferromagnetic layers sandwiching a non-magnetic layer. The resistance of device depends on the magnetization alignment of the ferromagnetic layers. Specifically, the device resistance is maximized when ferromagnetic layers are antiparallel aligned and minimized when magnetic moments in ferromagnetic layers are parallel. By pinning magnetization of one ferromagnetic layer (pinned layer) and changing magnetization of the other magnetic layer (free layer) by applying an outer magnetic field, a GMR device performs as a magnetic field sensitive

spin-valve, which is the key component in hard drive read-head. GMR read head be improved by material innovations in pinned layer and specular layer. In 1991, Parkin and Mauri reported a method of direct determination of ferromagnetic exchange coupling.[84] Instead of forming an interface that resists magnetization change by making a simple antiferromagnetic thin film on the pinned layer, they used a synthetic antiferromagnetic structure in which a Ru spacer layer is sandwiched between two ferromagnetic layers, one of which is pinned antiparallel to applied magnetic field. With optimized Ru interlayer thickness, strong antiferromagnetic coupling field is generated between ferromagnetic layers. Such exchange-coupling is thermally more stable than single pinned layer, resulting in improved operation temperature.[85] In addition, electron scattering loss can be decreased by adding a specular layer, usually oxide material, between free layer and capping layer. Consequently, electrons are reflected several times, reducing scattering loss and increasing GMR change.[86,87] Other GMR-based applications include current sensor, position sensor, and biosensors.[88]

The success of GMR results in rapid growth in magnetoresistance device research, including magnetic tunnel junction (MTJ), colossal magnetoresistance, etc. The MTJ device utilizes tunneling magnetoresistance (TMR) effect, which is related to tunneling effects of electrons between two ferromagnetic films that are separated by a thin insulating layer. Similar to GMR devices, the MTJ has antiparallel state of ferromagnetic layers corresponds to high tunnel resistance and parallel alignment corresponds to low resistance state. Although TMR has been observed as early as 1975, but reproducible TMR at room-temperature was only obtained until 1990s when aluminum oxide insulating layer based TMR were reported.[89-91] Compared to GMR

devices, MTJ has higher magnetoresistance (MR) ratio, which can be 70% at room temperature with optimized Al_2O_3 insulation layer fabrication conditions and ferromagnetic electrode materials.[92] In 2001, Mathon *et al*. predicted that the TMR ratio could be increased over 1000% for an MTJ with MgO insulating layer as thin as 20 atomic planes.[93] Later, Yuasa and Parkin obtained MTJ with MR ratio over 200%, in which single-crystal MgO (001) and textured MgO (001) were used as insulating layer, respectively.[94,95] More recently, MR ratio of 604% has been achieved in a CoFeB/MgO/CoFeB system.[96] The high MR ratio of MTJ device together with reduced lateral size makes it suitable for high-density hard-disk drive and magnetoresistive random access memory (MRAM). A MRAM system comprises of a transistor and a MTJ, and uses the magnetization state of free layer to represent data. Its nature of using magnetic switching instead of charge current enables infinite write endurance, lower power consumption, and long data retention.[97]

Besides research work on magnetoresistance-based devices, study on electrical spin injection, transport, and detection is also a critical topic in spintronics. Such technique is the key for exploiting electron spin in semiconductor systems. For example, spin field effect transistor has very promising potential in making low-cost non-volatile solid-state memory. In 1990, Datta *et al*. proposed a spin transistor structure made of a semiconductor channel and two ferromagnetic electrodes.[98] A spin-polarized current is injected into semiconductor channel from the source electrode, and detected by the drain current. The modulation of such spin current is achieved by gate voltage using Rashaba spin-orbit interaction.[99] Although theoretical studies on spin transistor made continuous

progresses in modeling and logic circuits design, the spin transistor structure proposed by Datta has yet to be realized.[100]

Another direction of spintronics research is the spin-based quantum computing. In quantum computing architecture, information is stored and processed by "qubits". A spin can be in a superposition of both up and down states and therefore can represent a qubit nicely. The following part will discuss quantum computing and electron spin as qubit in details.

3.1.2 Spin-based Quantum Computing

Quantum computing refers to computing based on quantum physics phenomena, for example superposition and entanglement. Different from the classical computation, which uses a non-quantum binary system that can be only one state at the time to interpret logical values, quantum computing uses a quantum bit that obey quantum mechanical principles as the basic unit for information storage and processing.[101,102] Such quantum bit can be in superposition of two states, therefore providing unique opportunities for breaking though barriers in classical computation, such as simulation in complex chemical systems, and information encrypt.[103]

The exploration of quantum information theory can be traced to 1964 when Bell proposed Bell's inequality based on the famous Einstein, Podolsky, and Rosen (EPR) paradox thought experiment. Bell demonstrated that the quantum mechanics has a much stronger statistical correlation with measurement results performed on different.[104] In the early 1980s, Paul Benioff proposed the quantum mechanical Hamilton models of Turing machines, and Richard Feynman suggested the possibility of building an advanced

computer based on a quantum system to perform simulation that is impossible for classical computers.[105,106] This speculative quantum computing system soon attracted considerable interest after Shor discovered an important algorithm that allows the system to quickly factor large numbers in 1994.[107] This is a critical progress since both factoring and discrete log problem were solved by Shor's algorithm. Shor also proposed the first quantum error correction scheme which was later experimentally realized with NMR qubits.[108,109] Although quantum algorithm theory became well understood, it is still a difficult task to build a quantum computer. This obstacle was overcome in late 1990s when Jonathan et al. claimed the first experimental implementation of a quantum search algorithm on a 2-qubit NMR quantum computer. The reported quantum computing system is faster than a comparable classical computer.[110]

As discussed above, the quantum computing relies on quantum bit, or qubit, for data processing. In principle, any two-state system can be used as a qubit. Researchers have explored various candidates for qubit, e.g. atomic spin, superconducting charge, and solid-state spin.

Atomic qubit is a qubit that utilizes atom energy levels to represent quantum information. Such qubits are homogeneous since the atoms of same chemical species are in principle identical. Therefore, an atomic qubit matches with one another in nature, resulting in simplified control requirement and less effort in building a large-scale quantum computing system.[111] A typical neutral atom quantum computer architecture comprises laser and microwave sources, time and space modulators, and qubit array.[112] First, the atoms are suspended in a vacuum chamber, being cooling by transferring atom

momentum to scatter laser. The laser-cooled atoms are confined by laser beams or magnetic fields and then encoded in hyper-Zeeman ground substates.[113] To date, the most studied materials for neutral atom qubits are Rb and Cs which are easy to be cooled and trapped. An alternative of neutral atom qubit is charged atom, or ion qubit. An ion can be trapped at saddle point by Paul trap, a radio frequency electric field trap proposed by Wolfgang Paul in the 1950s. In 1995, Cirac and Zoller proposed the first scheme of trapped ion computer. The cold ions are confined in a linear trap with laser beams, and quantum gates are enabled by ion coupling.[114] Based on this scheme, a considerable amount of progresses in trapped ion qubit control and entanglement has been made in the past two decades. For example. Harty et al. reported high fidelity operation of trapped $^{43}Ca^{+}$ ion, thus suggesting the trapped ion scheme can be used for building a universal quantum computer. The $^{43}Ca^{+}$ ion is chosen for making trapped ion computer since it has long coherence time (50 s) and its two hyperfine ground states are suitable for representing 0 and 1 states.[115,116]

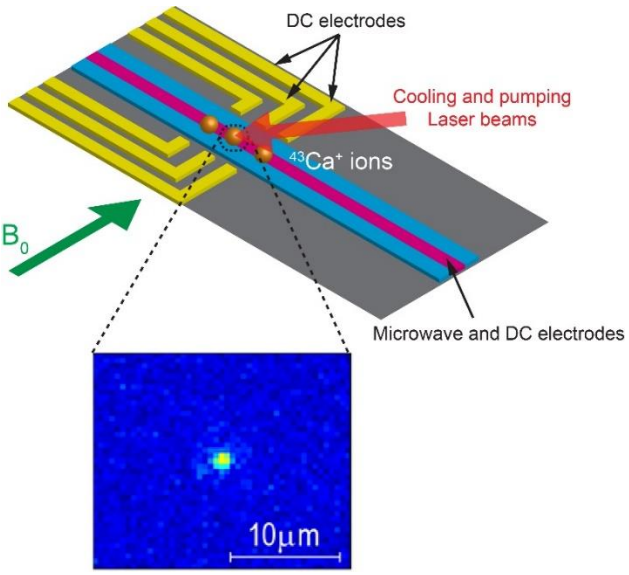

Figure 14. A trapped ion qubit made of $^{43}Ca^{+}$. The ion is confined in a trapping field by radio-frequency and DC electrodes and then cooled by laser beam. The qubit is prepared by the combination of laser pumping and microwave pulses. Applying various microwave signal combinations enables logic gate operations. Inset, qubit readout by fluorescence monitoring. Only "1" state generates fluorescence. Adapted from reference.[116]

In the reported scheme, a $^{43}Ca^{+}$ ion is trapped on a sapphire substrate by a Paul trap formed by neighboring electrodes. The trapped Ca ion is first engineered to well-defined initial ground state by laser pumping. Afterwards, on-chip microwave electrodes generate microwave pulses, which is combined with laser pumping, to prepare ion in 0 and 1 state. (see Fig. 14) The states can be readout by fluorescence accurately (average error rate as low as 0.07% for 150000 times readout). The hurdle of large-scale quantum computing using atomic qubits is the complexity in controlling modular connections. To build large-scale quantum computer, ions qubits are connected through a complex electrode system to avoid disturbance of qubit states. Ion moves between modules on an

electrical field wave generated by a large number of precisely positioned electrodes. Such design require very precise control over electrode voltages. An alternative way of scaling up atomic quantum computing is by photonic connection. However, the fact that photons needs capturing and guiding makes qubit-photon link inefficient.

An alternative to natural atomic qubit is to design artificial atoms using superconducting circuits containing Josephson tunnel junctions. A superconducting circuit, similar to natural atom, has discrete energy levels. At low temperature (millikelvin), the Josephson junction serves as a nonlinear circuit element. Thus, the lowest energy level in such nonlinear circuit can be addressed by external fields.[117] The superconducting qubit outstands natural atomic qubits in stronger coupling and tunability. Conventional integrated circuits fabrication techniques can be used to make this type of quantum circuits, which allows specific characteristics like particular transition frequencies to be integrated into circuit. In addition, the superposition state persistence is long enough for making a robust long-lifetime qubit at low temperature. The quantum mechanical behavior of superconducting qubits depends on two energy scales: the electrostatic Coulomb energy E_C, and the Josephson coupling energy E_J. Qubits can be implemented in three regimes of E_J/E_C, namely charge qubit, flux qubit, and phase qubit. (see Fig. 15) The charge qubit corresponds to $E_C \gg E_J$. In the circuit, two Josephson junctions couple the Cooper-pair box, which is a tiny superconducting island, to a superconducting reservoir. A voltage is applied though a gate capacitor to charge the box. The basis states of a charge qubit are charge states representing presence/absence of Cooper pair. The number of excess Cooper pairs tunneling across the Josephson junction determines the state of a charge qubit. Flux qubit, also known as persistent current qubit,

is in the regime $E_J \gg E_C$. It consists of a micrometer sized superconducting loop interrupted by several Josephson junctions. With an external magnetic field applied through the loop, a clockwise or counterclockwise persistent current flow is induced in the loop. The two lowest eigenstates of the loop represents the computational basis states of flux qubit. Phase qubit is also in the regime of $E_J \gg E_C$. It uses a current-biased Josephson junction and is operated at zero voltage state with bias current. The bias current generates phase difference of the two superconducting wave functions phases.

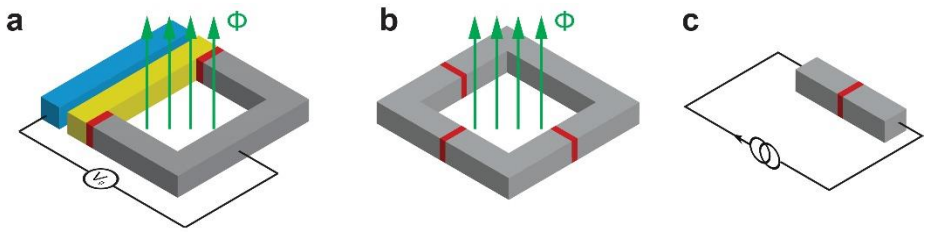

Figure 15. Schematics of superconducting qubit modalities. Red color represents Josephson junction. (a) A charge qubit implemented in the charge regime $E_C \gg E_J$. The loop consists of Josephson junctions (red), superconducting loop segment (grey), a Cooper-pair box (gold), and a gate capacitor (blue). The Cooper-pair box is biased by voltage V_g. The Josephson coupling energy is controlled by magnetic flux Φ. (b) Flux qubit, also controlled by flux Φ, is in regime $E_J \gg E_C$. Josephson junctions (red) separate the superconducting loop (grey). (c) A phase qubit uses Josephson junction biased by a large external junction. It is also in the $E_J \gg E_C$ regime but the ratio E_J/E_C is larger than flux qubit.

Such superconducting artificial atoms are proven successful platform for better understanding quantum mechanics and atomic physics in a way that is inaccessible with natural atoms. The past decade witnessed a great leap forward in superconducting qubit

research. Manipulation and entanglement of multiple superconducting qubit over long ranges have been realized through circuit quantum electrodynamics technique. However, the superconducting qubit is still limited by its low operation temperature and the significantly increased decoherence sources that affects performance at scaled level. To further improve the superconducting computing performance, further research on material and fabrication need to be conducted.

The third type of qubit is based on solid-state spin states. A spin can be in a superposition of both up and down states and therefore can represent a qubit nicely. Individual spins can be generated, manipulated in a stable solid-state source and detected by both electronic and optical techniques, thus offering many advantages over alternative quantum bit contenders.[118,119] The past 20 years have witnessed enormous progress in experimental studies in single spin initialization, control and detection, making the hypothetical experiments in the past become reality now.[120] The exploration of utilizing spin for quantum computing can be traced back to 1998 when Loss et al. for the first time proposed quantum computation based on the spin states of coupled single electron quantum dots.[121] At the beginning of this century, Hayashi et al. studied single-electron spin dynamics and demonstrated coherent manipulation of single-electron electronic states.[122] In 2005, Petta et al. managed to achieve coherent manipulation of coupled electron spins.[123]

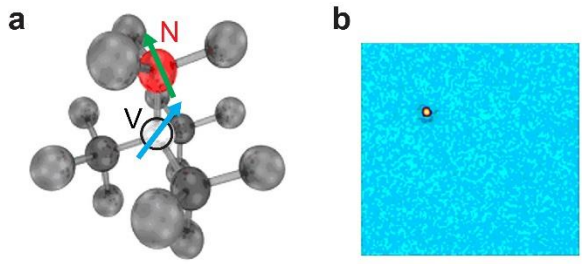

Figure 16. NV center in diamond. (a) Schematic of a nitrogen-vacancy defect, illustrating both the electronic spin at vacancy at nuclear spin on the nitrogen nuclei. (b) In confocal fluorescence image of CVD diamond, the fluorescence represents an individual NV defect. Figures adapted from reference.[124]

The tremendous progress in diamond growth and engineering in recent decade greatly promoted the studies of spins in diamond. Due to its long coherence times and unique optical properties, diamond has recently become a leading candidate for quantum bit control.[125-129] Most work of spins control in diamond focuses on nitrogen vacancy (NV) centers.[120] An NV center refers to one of the carbon atoms in diamond lattice replaced by a nitrogen atom and one of its neighboring site being empty. (See Fig. 16) Such impurities are attractive for coherent operation for two main reasons. First, single defect centers can be addressed by optical techniques. The electronic structure of the NV center allows generation of a spin in the ground state by optical illumination.[130] The initialized NV center spin can be manipulated by magnetic resonance and observed by scanning confocal optical microscopy because of its large dipole.[126] Second, NV center has long coherence times at both low temperature and room temperature. In 2009, Balasubramanian *et al*. studied the spin coherence time in diamond. The single electron spin in diamond showed longest spin coherence time observed in any solid-state system (T_2=1.8 ms) at room temperature. Based on these properties, the room-temperature

operation of coherent manipulation of spins have been demonstrated in diamond.[131-133] Compared to other quantum computing system such as superconducting Josephson junctions and phosphorus dopants in silicon, diamond-based spintronics has the primary advantage of capability of room temperature operation.

However, to date, the demonstrated NV center clusters are ultimately limited to a few spins. Large-scale quantum computing in diamond has not been achieved due to unable to perform spin states communication among large number of spin registers. Therefore, a method for realizing room-temperature large-scale quantum computing in diamond is greatly needed.

3.2 Spin Injection and Transport in Diamond

This project focuses on a unique solution to large-scale quantum computing, which is the carrier spin injection and transport in single-crystal diamond.

Spin injection is a critical research topic in spintronics as it offers great potential for non-volatile, high-speed devices as well as quantum information processing.[83] In 1990, Datta and Das proposed the first theoretical model of electrical spin injection into semiconductor materials.[98] Although extensive amount of effort have been made to realize the proposed injection model, the results achieved today are still very limited.[134] Researchers have studied various materials, including InAs, Si, and GaAs, and multiple injection methods, such as tunnel injection, ballistic electron injection. However, it is still a difficult task to achieve efficient spin injection due to short room-temperature spin coherent time, high spin-flip scattering and low transmissivity at interface.[135]

Diamond is expected to have long spin coherence time because of its unique physical properties, including low atomic number, small spin-orbit coupling (13 meV)[136], and inversion symmetry. Doherty et al. calculated the theoretical spin transport distance in diamond. At 100 V/cm electric field, this distance is ca. 2 mm.[137] Recently, Cardellino et al. reported transport of NV center spin in diamond.[138] However, there has been no demonstration of successful carrier spin transport in diamond.

All these properties make diamond an ideal spin transport material. Hence, this work aims at injecting spin-polarized current into doped high quality CVD grown single crystal diamond using mesoscopic ferromagnet electrodes. The diamond is epitaxially grown by Microwave Plasma Chemical Vapor Deposition (MPCVD). Robert Nemanich group helped with diamond growth on a 4 × 4 × 0.5 mm type II-a intrinsic CVD diamond (100) substrate. Before doped diamond growth, the substrates were chemical cleaned to eliminate metallic and organic contaminations. First, a hydrogen plasma pretreatment was applied to the substrate to prepare the surface for growth. For the B-doped diamond film growth, the carbon gas source was CH_4 diluted in H_2. B doping was carried out using trimethylborane (TMB) diluted in H_2. The detailed pretreatment and deposition condition is summarized in Table 1. With the parameters listed below, the anticipated thickness of the B-doped diamond epitaxy film is ca. 50 nm.

Table 1. Pretreatment and Growth Condition for (100) B-Doped Diamond Film

Process	H-Plasma	B-doped diamond deposition
Substrate temperature	750 °C	770 °C
Gas pressure	16 Torr	16 Torr
CH_4/H_2 ratio	-	0.4%
TMB/ CH_4 ratio	-	0.8%
Microwave power	1200 W	1200 W
Time	5 min	60 min

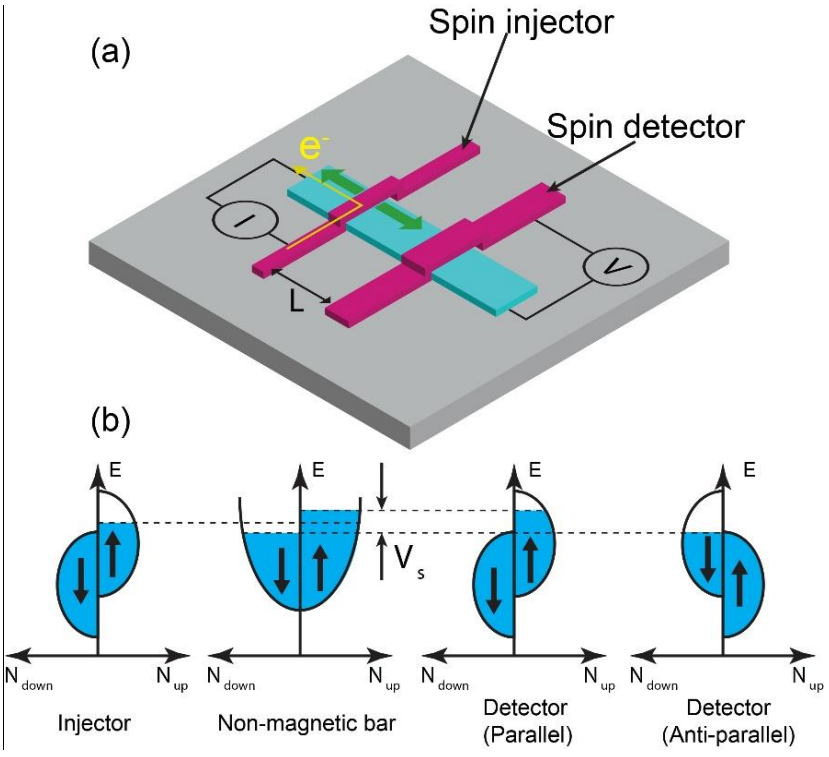

Figure 17. Schematics of lateral spin-valve working principle. (a) A lateral spin valve consists of non-magnetic bar (blue) and two ferromagnetic electrodes (magenta). A polarized charge current (yellow arrow)

was injected through injector electrode to non-magnetic bar. Thus non-equilibrium spin accumulation (green arrows) is induced in the bar and is measured by the detector electrode. (b) Band structures of ferromagnet and non-magnetic bar. For simplicity, the ferromagnet (injector and detector electrode) is represented by a half-metal band structure.

The key is to design a proper device for spin injection and detection. A lateral spin valve is proposed for such purpose. Fig. 17 illustrates the principles of a lateral spin valve, which consists of two laterally separated ferromagnetic electrodes with different widths and a non-magnetic bar. The band structures of these materials are illustrated by Fig. 17b. For simplicity, since the Fermi surface in ferromagnetic metal were completely in one spin sub-band, a half-metallic band structure is used to represent the ferromagnet. Suppose a spin-up polarized electric current driven from the injector electrode to the non-magnetic bar. The Fermi levels of the non-magnetic material then splits as non-equilibrium spins accumulate. The spin-up electrons correspond to higher Fermi level. The non-equilibrium spin accumulation induced by injection of polarized charge current decays exponentially as it diffuses away from the injector. This characteristic distance of spin diffusion is known as the diffusion length, l_s. It can be qualitatively described as the mean distance that electrons diffuse between spin-flipping collisions. The spin accumulation $\Delta\mu$ for a non-magnetic material[139] is given by

$$\Delta\mu = Ae^{-z/l_s} + Be^{z/l_s} \qquad \text{(Eq. 1)}$$

where z represents the distance from injection point. In Fig. 17a, as spins diffuse in both directions, a pure spin current exist on the right side of injector electrode, thus generating a potential difference. The detector electrode and non-magnetic bar then form a spin-sensitive voltage measuring circuit. In case of successful spin transport, a spin

signal V/I could be detected. The amplitude of such voltage is determined by the relative orientations of detector electrode spin and the transported spin. If these two spin orientations are parallel, then the Fermi level of ferromagnet electrode (detector) is aligned with the upper Fermi level in non-magnetic material, thus a higher voltage would be detected. When they are anti-parallel to each other, the Fermi level of detector is aligned with the lower level, which corresponds to a low voltage. The normalized voltage contrast[140] is given by

$$\Delta R = \frac{\Delta V}{I} = \frac{P_1 P_2 l_s \rho}{A} e^{-L/l_s} \quad \text{(Eq. 2)}$$

where L is the center-to-center distance between two magnet electrodes. ρ and A are the resistivity and cross junction area of non-magnetic material, respectively.

3.3 Devices Design and Fabrication

First, Hall bar device is designed for characterization of the carrier density and mobility in doped single-crystal diamond structures. As is shown in Fig. 18a, the Hall bar have two contacts (1,2) at both ends for applying current and four contacts (3,4,5,6) at sides for voltage measurement. The Hall Coefficient R_H is given by

$$R_H = \frac{V_H \cdot t}{B \cdot I} \quad \text{(Eq. 3)}$$

where V_H is the Hall Effect voltage (electric potential difference between 3,4 or 5,6), t is the thickness of diamond bar, B is the applied magnetic field along z direction, I is the current flowing through the diamond bar. Hall mobility (μ_H) and carrier concentration (n_H) could be calculated using Hall coefficient as

$$\mu_H = \sigma \times R_H \quad \text{(Eq. 4)}$$

$$n_H = \frac{1}{R_H \cdot e} \quad \text{(Eq. 5)}$$

where σ is the electrical conductivity of diamond bar, e is the charge of an electron. The desired length to width ratio should be at least 4:1. In the design, the Hall bar is a 500 × 50 μm large, ca. 50 nm thick doped diamond bar, with Ti/Au electrodes connecting contact points to external circuits bonding areas.

Second, a non-local lateral spin valve is designed. According to Doherty et al. calculation, the ideal spin transport distance in high-purity diamond is ca. 2 mm.[137] In practice, injector and detector electrodes should be placed at a significantly smaller distance due to the impurity scattering. As indicated by Eq.2, the spin accumulation decays exponentially with distance. Therefore, the electrodes gap should be designed to be as small as possible. In addition, increased gap could be tested to investigate the longest range that spin transport could be detected and the relation between spin signals vs. electrodes distance. The specific design of the lateral diamond spin-valve is illustrated by Fig. 18b.

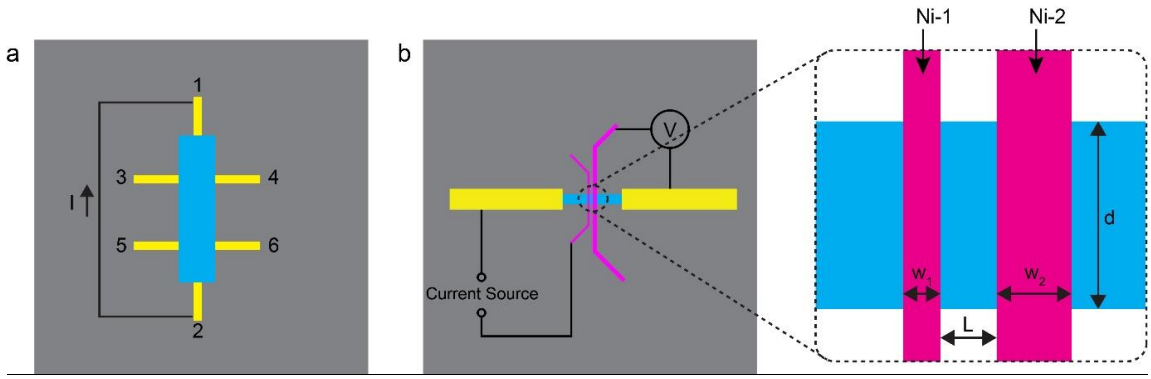

Figure 18. Design of Hall bar and spin-valve devices. (a) Hall bar is connected to six contacts. In Hall measurements, a current is injected through contact 1 and 2. Hall voltage can be measured by contact pair 3/4 or 5/6. (b) Spin-valve design. A doped diamond bar (blue) on intrinsic diamond substrate (gray) is connected to two Ni electrodes (magenta) and Au electrodes (Yellow). Inset: Zoom-in of ferromagnet electrodes on diamond bar. The Ni-1 is used for current injection and Ni-2 is used for spin signal recording. Their widths W_1 and W_2 are different so that their magnetic orientations flip at different magnetic field strength. L is the distance between the edges of these electrodes.

In the spin valve, a w_1=200 nm wide Ni ferromagnet electrode (Ni-1) and Au electrodes connecting to one end of a d=1 μm wide diamond bar forms a spin injection circuit to inject spin-polarized electrons into the diamond bar. At a distance L=300 nm from the injector, a second w_2=400 nm wide Ni electrode (Ni-2) is placed, which detects spin-polarized electrons in diamond bar. In addition, a lateral spin valve with larger separation distance (1000 nm) is designed to test the maximum spin transfer distance.

Delicate diamond-based nanoscale fabrication techniques are required to make structures proposed above. Since the diamond unique physical properties precludes traditional fabrication methods, a series of techniques that enable proposed

nanoelectronics devices made of high-quality single-crystal diamond have been developed.

First, mesoscopic electrodes have been successfully fabricated on diamond surface. EBL technique particularly designed for intrinsic surface of diamond was utilized to achieve patterning in such dimension ranges, followed by physical vapor deposition (PVD) metallization and lift-off process to complete electrodes. A 4 × 4 mm CVD diamond was spin-coated with triple layer E-beam resists. The first layer was Methyl methacrylate (MMA) which serves as an undercut layer for fine feature lift-off. The second layer was PMMA, the resist that accurately defines the pattern dimensions. A third layer of conductive polymer that can dissipate charges was coated for charge dissipation during EBL writing. The patterns of electrodes were fabricated under optimum electron dose and development conditions (Dose=700 $\mu C/cm^2$. Developed by a 3:1 mixture of Isopropanol and methyl isobutyl ketone for 90s). The scanning electron microscopy (SEM) images of the resulting patterns of 400, 200, and 70 nm lines and a spin-valve electrode pair pattern which consists of 200/400 nm electrodes with 330 nm separation are shown in Fig. 19.

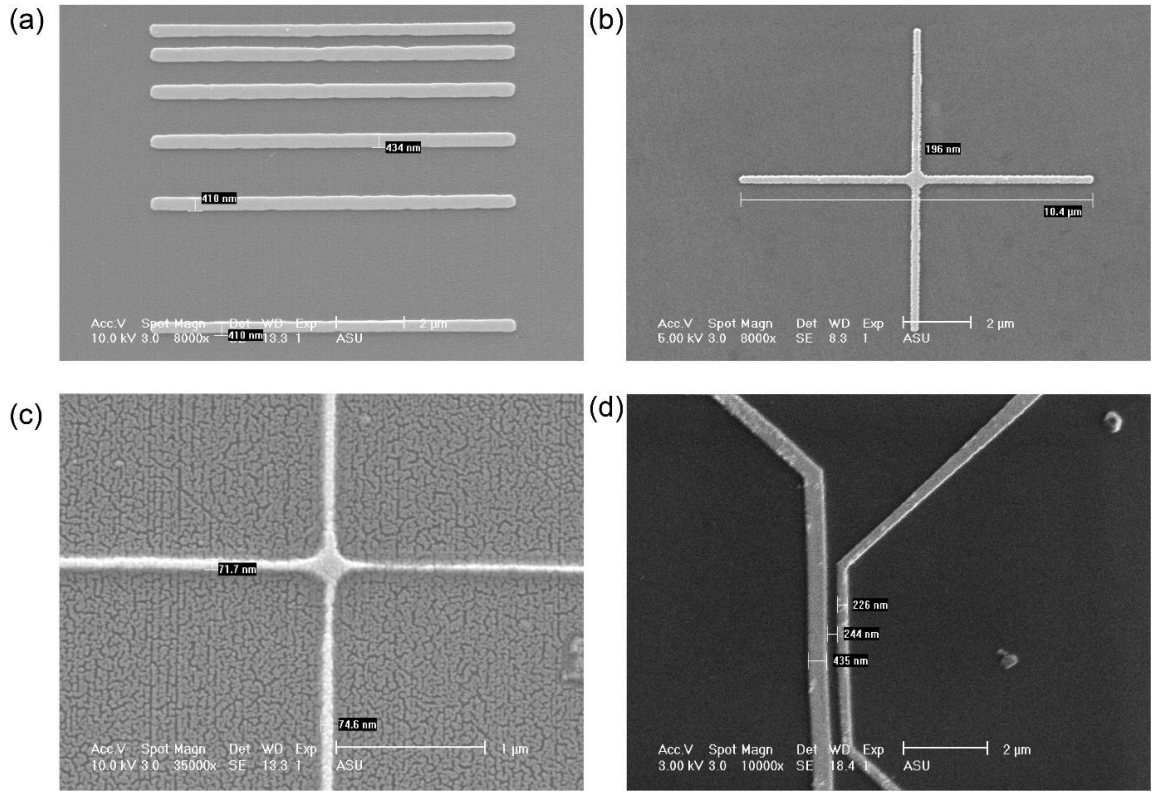

Figure 19. SEM images of electrodes fabricated on diamond substrates. (a) 400 nm parallel lines. (b) 200 nm cross pattern. (c) 70 nm cross pattern. The surface roughness came from sputtered Au coating for SEM imaging. (d) A spin-valve electrodes pattern that includes a 200 nm and a 400 nm electrode. The gap between them is ca. 330 nm.

In a spin valve device, the substrate is intrinsic, only the epitaxially grown top layer is the device layer for making the diamond bar for spin injection and transport. Therefore, the diamond bar is formed by etching the top doped diamond layer using RIE. CVD diamond etching with a reasonable rate and high selectivity was achieved in an RIE system. Fig. 20 illustrates the etching process of diamond. In stage (I), the etching mask pattern was defined using EBL writing technique as described above, followed by the sputtering of a 120 nm thick SiO_2 masking layer. In stage (II), the diamond surface was etched using a RIE system (Plasmatherm RIE 790) under 10 mTorr and 100 W RF

power. The flow rate of process gas O_2 was 20 sccm. The DC bias voltage was 380 V. Finally, in stage (III), the mask layer was removed by 2 min wet etching by Buffered Oxide Etch (BOE) solution. The etching rate and selectivity of diamond was calculated based on the thickness of layers measured by Dektak XT profilometer.

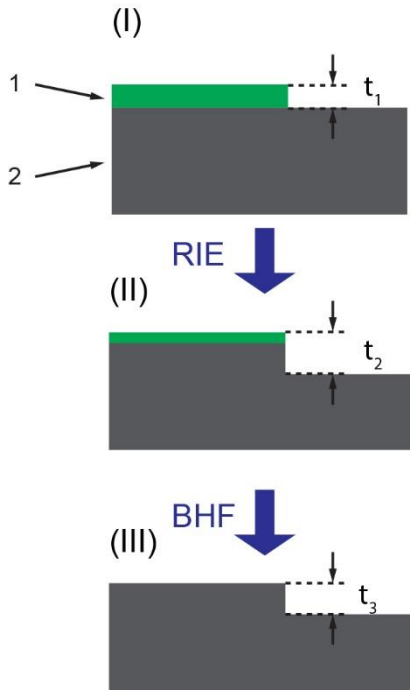

Figure 20. Schematics of diamond etching procedures. (I) The SiO_2 mask (1) is patterned on the diamond substrate (2) surface. The thickness of mask layer (t_1) is measured by profilometer. (II) The diamond is etched by an RIE process. The doped diamond layer is completely removed after RIE. Post-etch step height is given by t_2. (III) SiO_2 mask was removed by BHF etching. The depth etched into diamond is t_3. For clarity, the dimensions are not drawn to scale.

The diamond etch rate is given by

$$Rate = \frac{t_3}{time} \quad \text{(Eq. 6)}$$

where t_3 is the etched depth into diamond. (See Fig. 20) The etch rate was ca. 11 nm/min.

The selectivity for etching rate is given by

$$Selectivity = \frac{t_3}{t_1 - (t_2 - t_3)} \quad \text{(Eq. 7)}$$

where t_1 refers to the thickness of SiO_2 mask before etching, t_2 is the total thickness of mask and etched diamond structure underneath the mask after etching, and t_3 refers to etched diamond structure's height. The selectivity for SiO_2 mask is ca. 8.

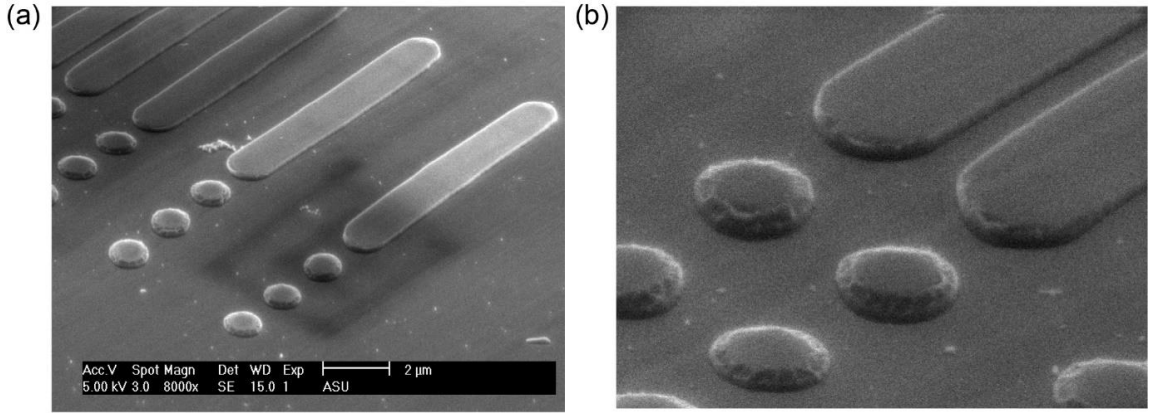

Figure 21. SEM graphs of diamond structures etched by RIE. The mask layer has been removed post-etching. (a) SEM of etched structures. The array consists of 1 × 10 µm stripes and ⌀ =1 µm dots. (b) Zoom-in of etched diamond structures.

The spin-valve structure proposed in this work requires making a diamond bar of which the width is as small as 1 μm. Such features have been successfully fabricated by etching method discussed above. The surface morphologies of the etched diamond structure are shown in Fig. 21. It is clearly shown that 1 × 10 μm bars and ⌀ =1 μm dots can be etched with smooth etch surfaces. The depth etched into diamond is ca. 150 nm.

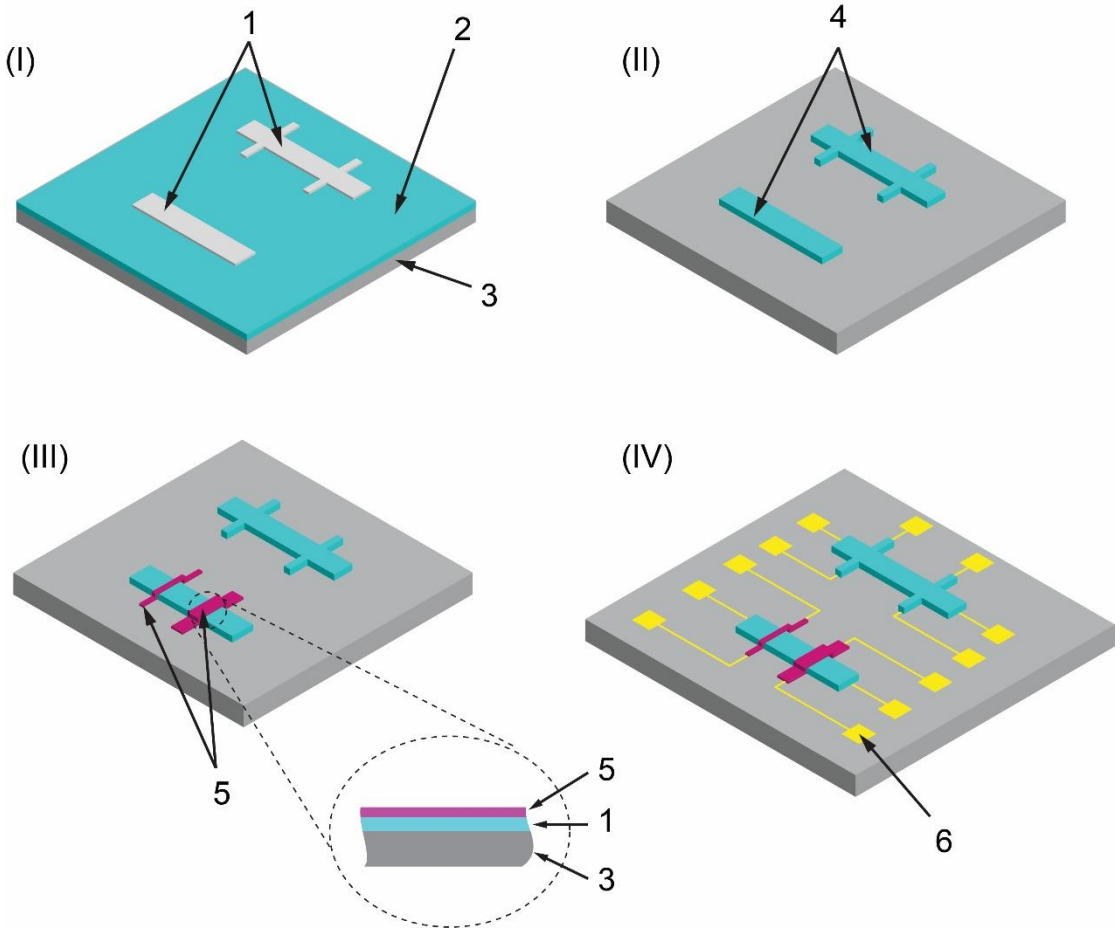

Figure 22. Schematics of Hall bar and lateral spin-valve fabrication procedures. For clarity, the dimensions are not drawn to scale. (I) SiO_2 masks (1) are deposited on the doped diamond layer (2) which is epitaxially grown on an intrinsic diamond substrate (3). (II) Hall bars and spin valve diamond bars (4) are carved out using RIE, followed by the removal of the SiO_2 masks. (III) Ni electrodes (5) are fabricated on top of

diamond bar by EBL techniques. Inset, cross-section of Ni electrodes, doped diamond, and intrinsic diamond substrate. (IV) Au interconnects and bonding pads (6) are patterned on diamond surface.

The fabrication procedures for the Hall bar and lateral spin valve are illustrated in Fig, 22. Firstly, a set of SiO_2 masks (1) defining patterns for the semiconductor diamond bars is fabricated by EBL and PVD. Second, the diamond bar (4) is carved out by RIE procedures. During the RIE, the SiO_2 masks protect the diamond bar while the uncovered doped diamond is completely removed, leaving bare undoped diamond (3) on the surface. Then two 90 nm thick Ni electrodes (5) will be defined on the etched diamond bar, serving as the ferromagnet spin injection and detection electrodes. Finally, Au bonding pads and circuit interconnects (6) is fabricated (Ti/Au=5/100 nm).

3.4 Results

3.4.1 Hall Bar Characterizations

The optical microscope image of the as-fabricated Hall bar is shown in Fig. 23 a. A 50 × 500 μm, ca. 50 nm thick Hall bar is connected to six gold contacts (Ti/Au=5/100 nm). Each contact leads to a 200 × 400 μm large bonding area. First, to verify that the doped diamond has been completely removed and the only conductance is from the diamond bar, the conductance of the etched diamond surface was measured. Two neighboring bonding areas, A and B, were used for measurement. The gap between these two pads are 50 μm, which is the smallest among all bonding pads. They are connected to different Hall bars. Therefore, there should be no conductance between these two pads.

The instruments used for measurement are a probe station and Keithley 2636B Source Meter SMU instrument. The data were obtained using a customized program run on Igor Pro. To measure the conductance, two probes are directly contact with bonding areas A/B. The I-V relation is acquired by recoding the resulting current while applying voltage up to 5 V. (See Fig. 23 b) The result indicates there is no conductance between bonding area A and B, and the etched surface is intrinsic.

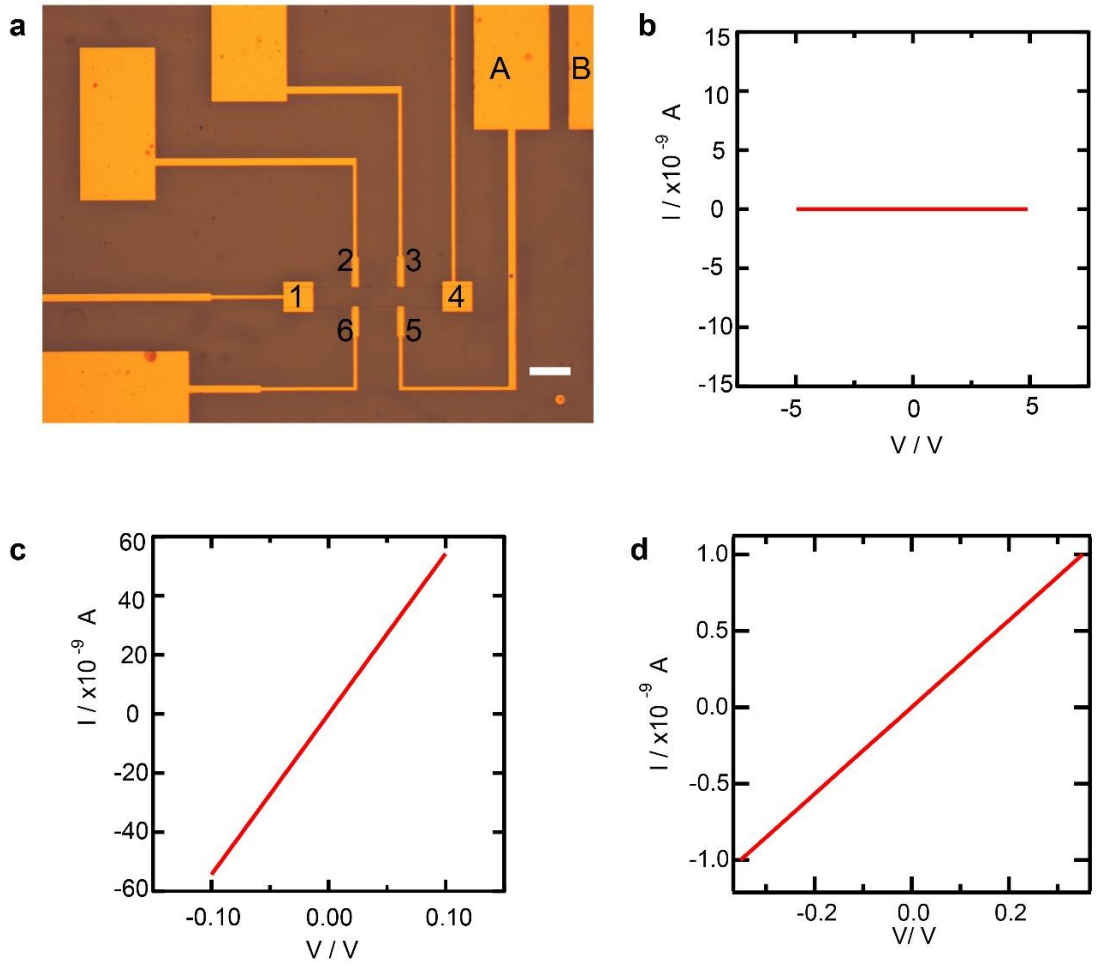

Figure 23. Characterizations of Hall bar at room temperature. (a) In total six contacts are connected to the Hall bar. 1,4 are used for current injection. 2,3,5,6 are used for Hall Effect and magnetoresistance measurements. Scale bar, 100 μm. (b) Surface conductance test using bonding areas A and B, which are

bonding areas of different Hall bar devices. (c) Current voltage characteristics measured using contact 1 and 2. (d) Conductivity measurements using contact pairs 1/4 for current injection and 2/3 for voltage measurement.

Next, the Hall bar device was evaluated by current voltage characterization at room temperature to calculate conductivity. The measurement setup is the same for conductance measurement described above. The probes are contacted with bonds areas that lead to contacts on the Hall bar. A sweeping voltage between -0.1 to 0.1 V was applied. The I-V characteristics of the Hall bar measured by contact pair 1-2 is shown by Fig. 23 c, respectively. The linearity of I-V characteristics reveal the ohmic properties of the device. The conductivity was evaluated using four probe method: a current is applied through contact pair 1/4 and resulting voltage between 2 and 3 is measured to calculate the conductivity using equation

$$\sigma = \frac{l}{A} \cdot \frac{I}{V} \qquad \text{(Eq. 8)}$$

where l is the length of the diamond bar, A is the cross-section area, V and I are voltage applied and resulting current. The calculated average conductivity is $\sigma = 85\ S/m$.

In addition, to characterize the carrier concentration and mobility, the Hall voltage and magnetoresistance were tested. This experiment was conducted at room temperature. The measurement system, provided by Dr. Tingyong Chen, consists of an electromagnet capable of generating magnetic field up to 1500 Oe, a customized probes station, and a Keithley SMU. The specimen is mounted on a holder above the magnet so that the magnetic field is vertical to the plane of Hall bar. Data management was performed by

customized LabVIEW program. First, the Hall voltage measurement is performed. Contact 1 and 4 (see Fig. 23) are used for injecting a constant current I_x, and the Hall voltage is measured by contact 2 and 6 while sweeping magnetic field from -1500 Oe to 1500 Oe.

3.4.2 Hall Voltage and Magnetoresistance Measurements

The Hall bar device was then mounted onto a customized probe station which provides magnetic field for Hall voltage and magnetoresistance measurement. In principle, the voltage difference across the Hall bar (measured by contact 2 and 6) should be zero when there is no magnetic field. As a vertical magnetic field is applied, charge carriers, driven by Lorentz force, are deflected toward one side of the Hall bar. The resulting accumulation of carriers thus generates a transverse electric field. This electric field counteracts with the Lorenz force by the magnetic field. Finally a steady-state is reached when these two forces are balanced. At such state, the potential difference due to transverse electric filed is the Hall voltage. Therefore, the plot of Hall voltage vs magnetic field should be a linear curve which passes through the origin point. The results of Hall voltage measured at $I_x = 5\ \mu A$ and $I_x = 10\ \mu A$ are illustrated by Fig. 24a and 24b, respectively.

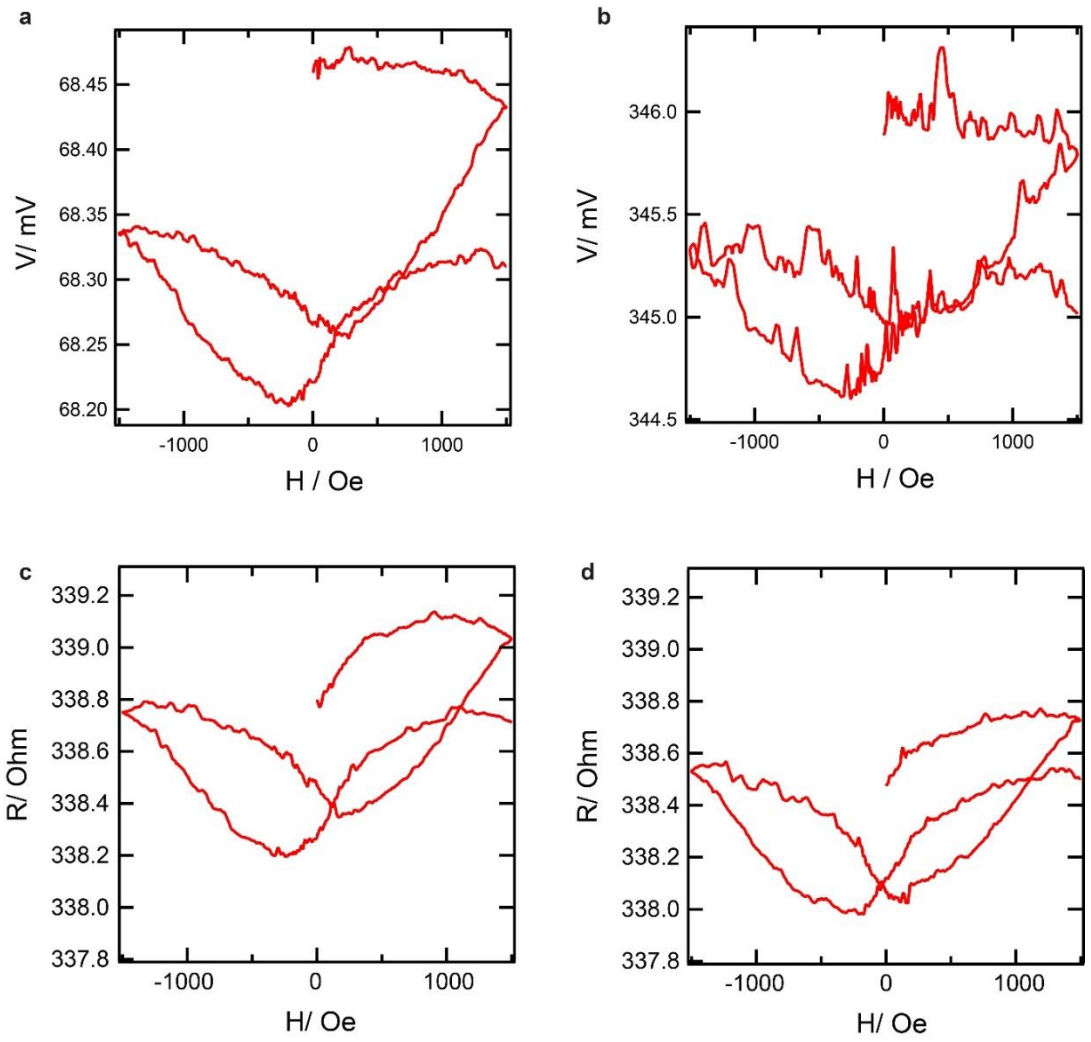

Figure 24. Hall Effect measurements. (a) Hall voltage with $I_x = 2\ \mu A$. (b) Hall voltage measurement with $I_x = 10\ \mu A$. (c) Magnetoresistance measurement with $I_x = 2\ \mu A$. (d) Magnetoresistance measurement with $I_x = 5\ \mu A$.

The preliminary results were different from the theoretical prediction. Firstly, the curves recorded did not pass through the coordinate origin. In other words, the voltage across Hall bar is not zero when no magnetic field is applied. Second, although the voltage increased with magnetic field strength when B>0, the expected linear relation

was not observed when B<0. The observed voltage at B=0 can be explained in part by the possible misalignment of electrodes. In design, the contacts 2 and 6 are in the same position along y direction (longitudinal direction of Hall bar). In case that 2 and 6 are not aligned well in fabrication, a gap along the y direction between these two contacts could be created, resulting in a potential difference when current I_x is injected. However, the reasons for voltage change with magnetic field are not yet completely understood. Magnetoresistance is measured by injecting constant current through contact 1/4 and recording voltage from contact 2/ 3 while sweeping magnetic field. The Fig. 24c and 24d present measurement results at $I_x = 2\ \mu A$ and $I_x = 5\ \mu A$, respectively. Remarkably, it was observed that the resistance changed with magnetic field. This observed magnetoresistance implicates that the external magnetic field changed diamond electrical resistance. It is very likely that, at room temperature, the Hall Effect is not strong enough to be observed, but still causes slight change in electrical resistance (<1%). Future low-temperature Hall Effect measurement are needed to estimate the carrier mobility.

3.4.3 Spin-valve Devices Characterizations

Two spin-valve devices are fabricated according to the design proposed in Section 2.3. One of the devices has smaller Ni electrodes widths (200/400 nm) and narrower gap (L=300 nm). The other is made with larger Ni electrodes sizes (1000/2000 nm) and wider gap (L=1000 nm). Fig. 25 presents the spin-valve with smaller Ni electrodes. In this device, a barbell-shaped diamond bar with two 10 × 15 μm contact pads and a 1 × 40 μm bar serves as the medium of spin transfer. Two Ni electrodes are used for injecting and detecting spin-polarized currents. The components of spin valve is connected to circuits at electrode sites 1-6. To check the circuits are properly connected at these sites, a series

of current voltage characterizations were conducted at room temperature using probe station and Keithley SMU. First, the diamond bar is tested by sweeping voltage from -1 to 1 V and recording resulting current. The result indicates semiconducting properties of the diamond bar. (see Figure 25b) Next, the resistance of the two Ni electrodes were measured to verify they are intact and the circuits are closed. In addition, the spin-injection loop is also checked. As shown in Fig. 25e, the circuit is closed, indicating that Ni electrode, diamond bar, and gold electrodes are properly connected. Last, the conductance of the spin-transfer loop which includes a 300 nm long diamond bar segment was tested. As is shown Fig. 25f, the conductance of this loop is relatively low. The low level of conductance should be attributed to low conductance of short segment of semiconducting diamond and high resistance at the contacts between diamond and Ni electrodes.

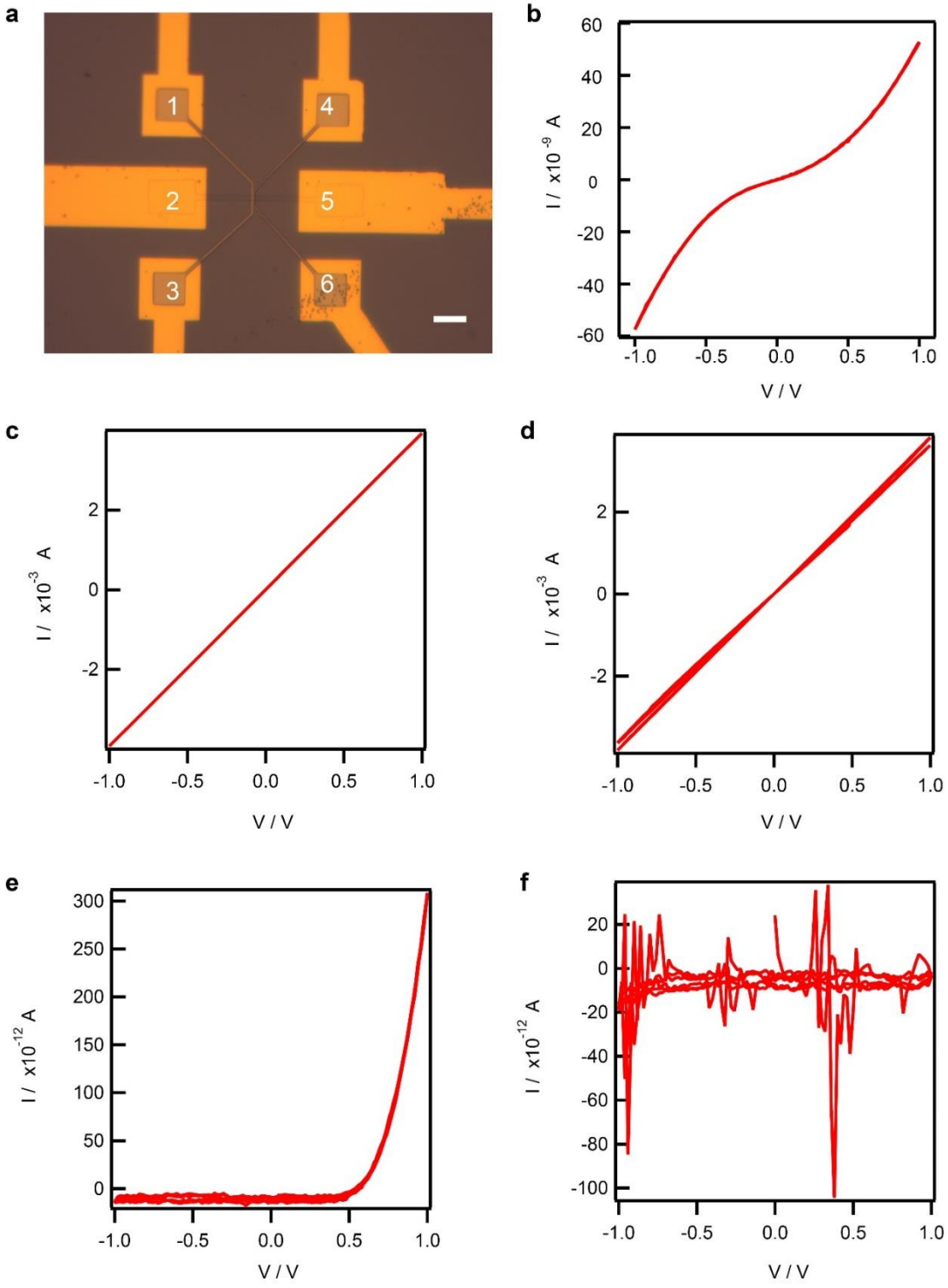

Figure 25. Image and characterizations of spin-valve device with 200/400 nm Ni electrodes. (a) Optical image of spin-valve device. A 1 × 40 μm diamond bar with 10 × 15 μm contact pads at its two ends is

connected to gold electrodes 2 and 5. Two Ni electrodes are fabricated on top of the diamond bar. They are connected to the spin injection/detection circuit at electrode site 1/3 and 4/6. Scale bar, 10 μm. (b) Current voltage characterization of diamond bar using contact 2 and 5. (c) Current voltage characterization of 400 nm Ni electrode using contact 1 and 3. (d) Current voltage characterization of 200 nm Ni electrode using contact 4 and 6. (e) Characterization of spin injecting circuit using contact 4 and 5. (f) Characterization of spin transport circuit using contact 3 and 4.

The second spin-valve was examined using the same methodology for testing the smaller spin-valve. (see Figure 26) The results clearly show that the Ni electrodes and diamond bars are intact and properly connected. Compared with the other spin valve, this device show significantly higher conductance of the spin injecting and transfer circuits. The increased conductance is resulted from large contact area between diamond bar and Ni electrodes, and longer diamond bar segment. Interestingly, two symmetrical rhombus shapes appear in the current voltage characteristics of diamond bar.

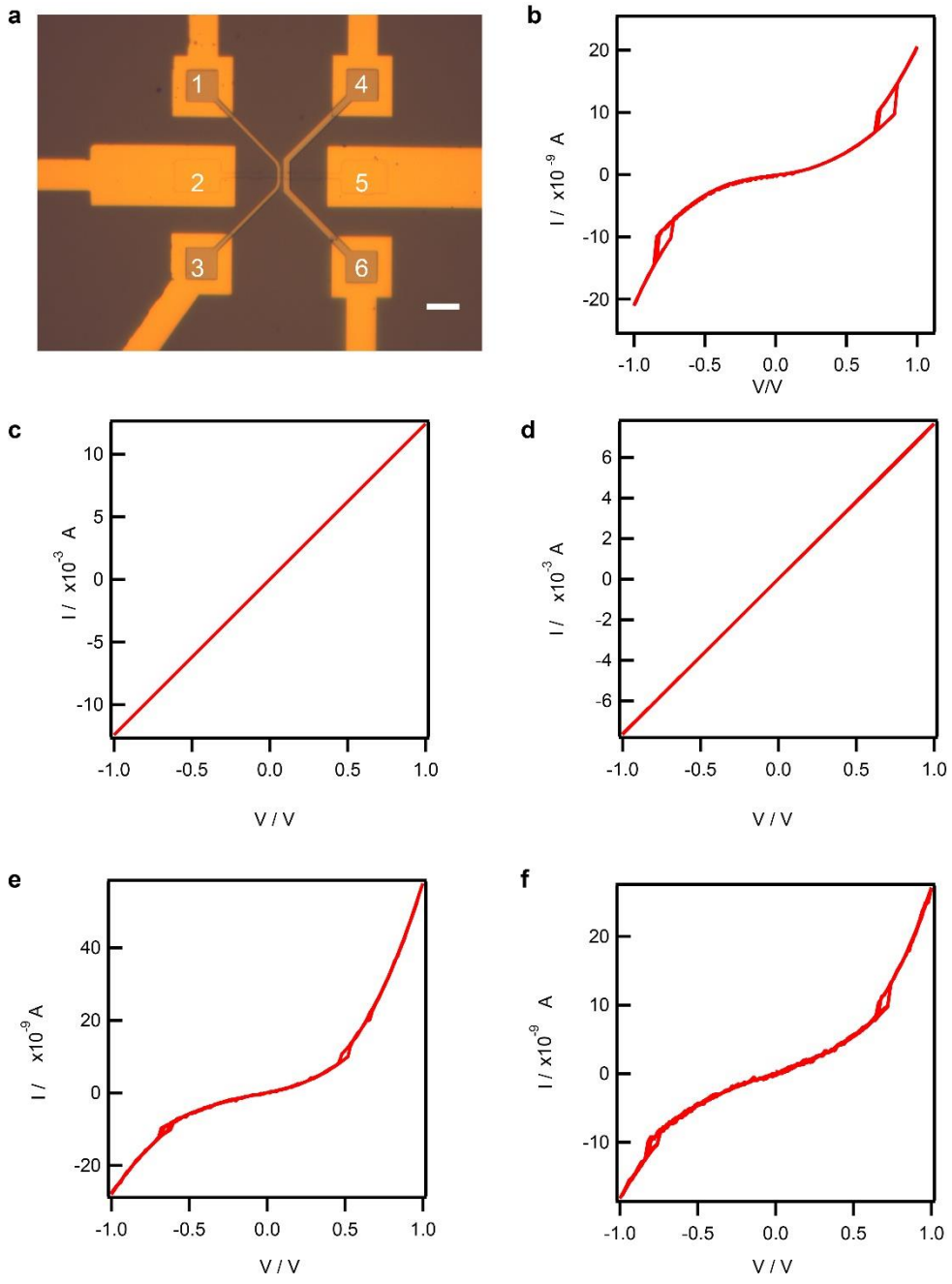

Figure 26. Image and characterizations of spin-valve device with 1000/2000 nm Ni electrodes. (a) Optical image of spin-valve device. A 1 × 40 μm diamond bar with 10 × 15 μm contact pads at its ends is connected to gold electrodes 2 and 5. Two Ni electrodes are fabricated on top of the diamond bar. They are connected to the spin injection/detection circuit at electrode site 1/3 and 4/6. Scale bar, 10 μm. (b) Current voltage characterization of diamond bar using contact 2 and 5. (c) Current voltage characterization of 1000

nm Ni electrode using contact 1 and 3. (d) Current voltage characterization of 2000 nm Ni electrode using contact 4 and 6. (e) Characterization of spin injecting circuit using contact 4 and 5. (f) Characterization of spin transport circuit using contact 3 and 4.

There are several possible explanations for this phenomenon. First, this phenomenon could be explained by the speculation that the injected current pushes the domain wall, resulting in a hysteresis in the IV curve. Future work needs to be done to further verify this speculation theoretically and experimentally. Another explanation is that this is due to partial Schottky barrier. Since the diamond surface could be affected during fabrication steps, a partial Schottky barrier could exist in the diamond and Ni contact area, thus results in the observed rhombus shapes in I-V characteristics.

3.4.4 Spin Signal Measurements

The spin injecting and transport in diamond is examined by the spin-valve device with L=1000 nm. The diamond sample was mounted on a carrier that has metal leads connected to the bonding pads on diamond. (see Fig. 27a) In order to perform low-temperature measurement, this carrier was fixed on a vacuum sample tube where liquid helium was introduced.

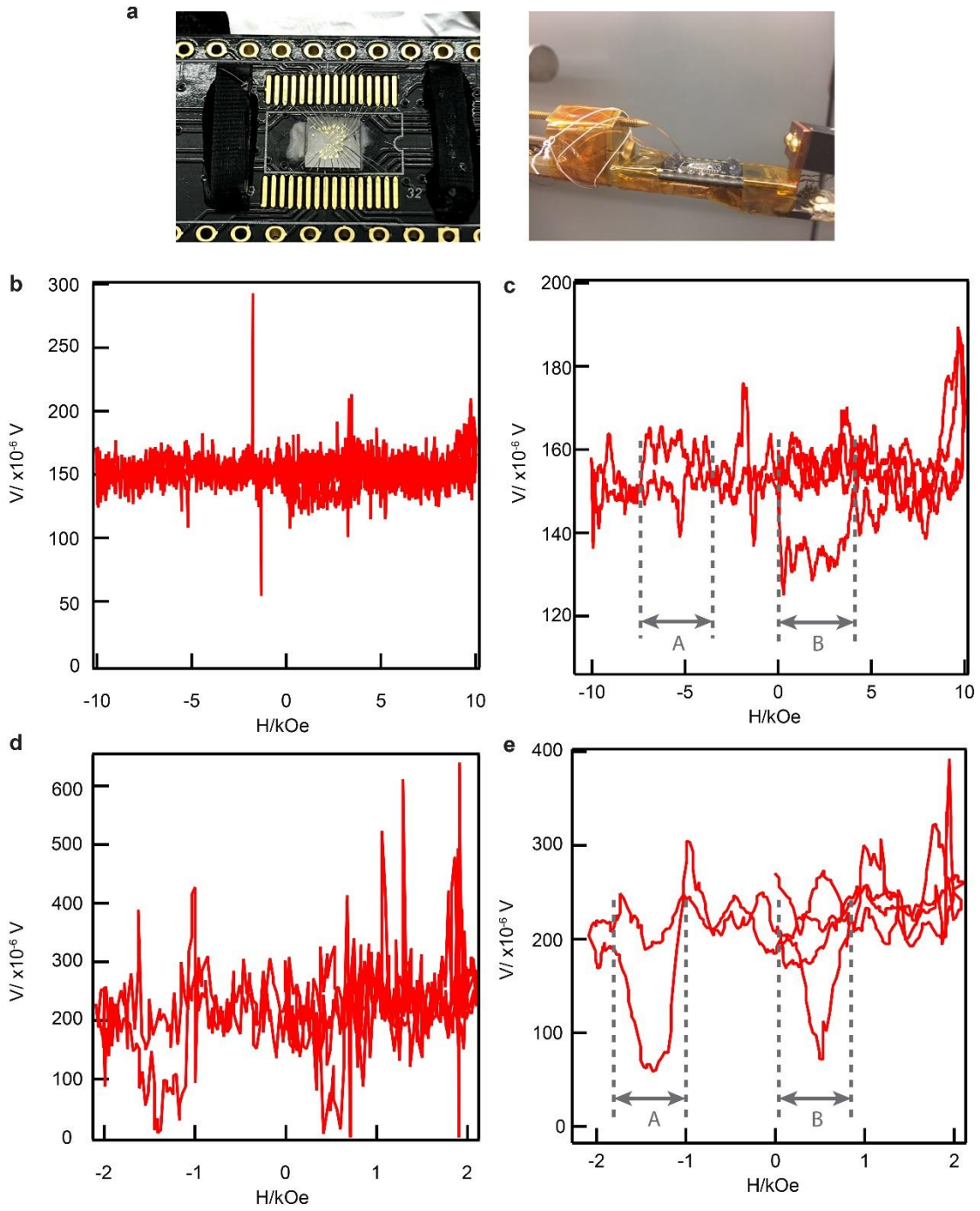

Figure 27. Spin signal measurements. (a) The diamond sample was mounted on a carrier using PMMA and thermal paste. Metal pads on the sample were bonded to leads on the carrier, which were connected to measuring units. The carrier was then sealed in a sample tube where liquid helium was introduced. (b) The original spin signal of a spin valve with L=1000 nm at 4.5 K. Injected current I=10 μA. (c) Spin signal in

(b) is smoothed by a box filter (m=3). (d) The spin signal of the device measured with injection current I=50 μA at 4.5 K. (e) Spin signal in (d) is smoothed by a box filter (m=3).

The 2000 nm Ni electrode (injector) and diamond bar were connected to a current source (by contact 4, 5 in Fig. 26) which provided injection current I. The 1000 nm Ni electrode (detector) and diamond bar were connected to the voltage measuring unit (by contact 2, 3 in Fig. 26) to give the voltage readout V. To determine the effect of an in-plane magnetic field, a magnetic field B whose direction is parallel to the long axes of Ni electrodes was applied. The spin signal V was monitored while sweeping the magnetic field from -10 kOe to +10 kOe. Such measurement was performed at 4.5 K. The spin signal V was analyzed by plotting it versus in-plane magnetic field B (see Fig. 27b). The data showed that the spin-polarized current was transported via diamond bar, resulting in a voltage contrast between detector electrode and diamond bar. Since the measurement system was originally designed for testing metallic materials, the impedance of contacts are higher than semiconductor measurement apparatus, resulting in significantly higher noise level. Therefore, the original data was then smoothed using a Box Filter (m=3) through Igor program (see Fig. 27 c). It is clear that, in the smoothed data, there exist signals that are significantly larger than the noise level, and these are considered to be the voltage contrast change caused by magnetization flip. This phenomenon agrees with the theoretical prediction that the two ferromagnetic electrodes switch their magnetic orientation at different magnetic field strength and exhibit two voltage states. With higher injecting current, such two-state phenomenon is more obvious. As shown in Fig. 27e, the percent change of spin signal is ca. 70%. These measurement records are the evidence of

carrier spin transport in diamond. The two-state spin signal are due to parallel and antiparallel alignment of the two ferromagnetic electrodes.

3.5 Discussions and Future Work

To sum up, spin injection and transport in epitaxially grown single-crystal diamond have been investigated, which is believed to be a unique solution to large-scale quantum communication in diamond, and presented preliminary evidence of spin transport in diamond nanoscale device. Specifically, a series of delicate fabrication techniques that enable nanoelectronics devices based on high-quality diamond was developed, including Hall bar device for material characterization and non-local lateral spin-valve devices for spin-polarized current injection and spin signal detection. Spin signal, which is the voltage contrast induced by spin transport in diamond, was obtained. And it was observed that the spin signal changed with magnetic field. Taken together, these findings implicate a blueprint for a new way to achieve large-scale quantum information processing using diamond spintronics.

This work clearly has some limitations. Firstly, although magnetoresistance of the Hall bar was recorded, the precise measurement of carrier mobility and concentration is still incomplete. Future experimental investigations are needed to examine the Hall voltage using a Hall bar device at low temperature. The Hall bar sample will need to be bonded onto a carrier and kept in a sample tube inside Helium tank. More significant Hall voltage is expected under lower temperature.

In addition, the spin injection and detection device could be further developed to explore diamond spintronics in various ways. For example, tunnel barriers made of Al_2O_3 could be added between ferromagnet and diamond bar as they provide a high spin dependent resistance that could enhance the spin polarization of injected current. (see Fig. 28a)

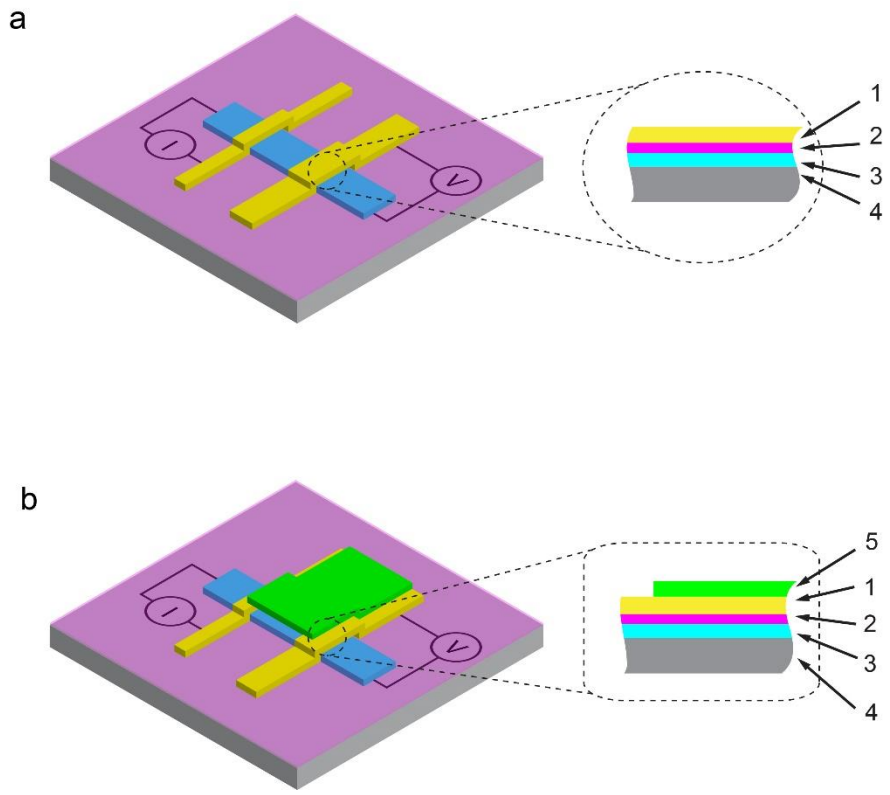

Figure 28. Proposed alternative spin injection models. (a) Tunnel injection model. A thin layer of Al_2O_3 is added between ferromagnetic electrode and diamond bar. Inset: cross-section of the device structures at ferromagnet contact. The ferromagnet electrode (1) is separated from the doped diamond bar (3) by an insulating material layer (2). The diamond substrate (4) is intrinsic. (b) Gate-controlled tunneling spin injection model. Inset: cross-section of device. The doped diamond bar (3) on intrinsic diamond substrate (4) is separated from ferromagnet electrode (1) by insulating layer (2). The gate electrode (5) is fabricated on top of ferromagnet electrodes to control the tunneling current.

In a tunneling injection model, a thin layer of tunnel barrier is deposited to the sample surface by PVD after the doped diamond bar is carved out by RIE. Then the ferromagnetic electrodes are patterned and evaporated on top of this layer. Different tunnel barrier materials can be tested, including Al_2O_3, h-BN, or Si_3N_4. A gate controlled tunneling model can also be tested in the future. (see Fig. 28b) This model of injection allows the control of tunneling current by the additional gate electrode. In summary, this work will serve as a base for future studies on spin injection and detection in diamond.

In addition, spintronics has great potential to be used as biomedical signal detection platforms, single molecule actuators, and magnetoresistive diagnostic platforms. The unique combination of the probe, which can deliver core functional structures into deep tissue with minimal damage, and diamond spintronics, makes it possible to develop implantable diamond-based spintronics biosensors.

4. CONCLUSIONS

This dissertation focuses on material and structure innovation for novel nanoelectronics devices. Specifically, I have worked on (1) the integration of biodegradable sacrificial layers for accurately implantable bio-probes, and (2) Hall bar and spin valve devices on epitaxially grown single crystal diamond.

In Chapter 2, novel biodegradable sacrificial layer integrated probes were developed to solve the problem of reconciling rigidity and flexibility in implantable probe. For long-term biocompatibility and performance, implanted probes need further reduce their size and mechanical stiffness to match that of the surrounding cells, which, however, makes accurate and minimal invasive insertion operations difficult due to lack of rigidity, and brings additional complications in assembling and surgery. Existing improvements in probe design can address some of the constraints but typically not all of the constraints without resulting in limitations in abilities, or bringing additional complexities in assembly and surgery. To overcome this barrier, novel designs of ultra-flexible probes utilizing biodegradable sacrificial layer and corresponding surgery procedures to deliver probes accurately into tissue-mimicking gel were proposed. Briefly, the integrated biodegradable sacrificial layer can dissolve in physiological fluids shortly after implantation, which allows *in situ* formation of functional ultrathin film structures off the initial small and rigid supporting backbone. It was shown that the dissolution of this layer does not affect the viability and excitability of living neuron cells *in vitro*. A high yield (>93%) of the bend-up structure was obtained and its geometry and stiffness can be systematically tuned. The robustness of the ultra-flexible probe has been tested in tissue-mimicking agarose gels with <1% fluctuation in the test resistance.

In Chapter 3, preliminary investigations into spin injection and characterizations of electron/hole spins in single crystal diamond were demonstrated. Diamond is a widely studied solid-state platform for spin-based quantum devices. The optically addressable spins in nitrogen vacancy (NV) centers in diamond have the longest spin coherence time (2 ms) of any solid-state system at room temperature, and therefore, they have attracted most attention to realize small-scale quantum information processing. However, large-scale quantum computing still faces a major barrier of the communication between the spin states of large number of NV centers. Electron/hole spin in diamond devices, on the other hand, could also be a good candidate for quantum computing due to the very small spin-orbit coupling in diamond and great coherent transport length of spin. However, demonstration of carrier spin transport in diamond has yet been achieved because of difficulties in diamond growth and nanofabrication of diamond. In this work, the potential of using diamond for spin injection, transfer, and characterization was explored by making nanoelectronics devices on a single-crystal diamond sample: a Hall bar device was used for material characterization, and a lateral spin valve for spin-polarized current injection. Fabrication processes for building doped diamond bar structures and for precisely aligning and constructing ~100 nm scale electrodes and channels on diamond substrates were developed. Preliminary evidence of successful spin injection and transport in diamond were obtained.

To sum up, this research work focuses on innovating materials and structure designs for functional nanoelectronics. The novel fabrication strategies and the understanding of the mechanical, chemical, and electronic properties of devices in these two projects could lead to new biomedical practices and new building blocks for quantum

computing, and, more interestingly, the possibility of bringing spintronic devices into biological systems as highly sensitive probes.

REFERENCES

1. Jiao, X.; Wang, Y.; Qing, Q. *Nano Lett.* **2017**, *17*(12), 7315–7322.

2. Kook, G.; Lee, S.; Lee, H.; Cho, I.-J.; Lee, H. *Micromachines* **2016**, *7*(12), 179.

3. Scholten, K.; Meng, E. *Lab Chip* **2015**, *15*(22), 4256–4272.

4. Calabresi, P.; Centonze, D.; Bernardi, G. *Trends Neurosci.* **2000**, *23*.

5. Limousin, P.; Krack, P.; Pollak, P.; Benazzouz, A.; Ardouin, C.; Hoffmann, D.; Benabid, A.-L. *N. Engl. J. Med.* **1998**, *339*(16), 1105–1111.

6. He, W.; Mcconnell, G. C.; Bellamkonda, R. V. *Journal of Neural Engineering* **2006**, *3*(4), 316–326.

7. Wojtecki, L.; Moldovan, A.-S.; Groiss, S.; Elben, S.; Südmeyer, M.; Schnitzler, A. *Neural Regeneration Research* **2015**, *10*(7), 1018.

8. Lebedev, M. A.; Nicolelis, M. A. *Trends in Neurosciences* **2006**, *29*(9), 536–546.

9. Altuna, A.; Bellistri, E.; Cid, E.; Aivar, P.; Gal, B.; Berganzo, J.; Gabriel, G.; Guimerà, A.; Villa, R.; Fernández, L. J.; Prida, L. M. D. L. *Lab on a Chip* **2013**, *13*(7), 1422.

10. Nicolelis, M. A. L. *Nature Reviews Neuroscience* **2003**, *4*(5), 417–422.

11. Nowlis, D. P.; Kamiya, J. *Psychophysiology* **1970**, *6*(4), 476–484.

12. Chapin, J. K.; Moxon, K. A.; Markowitz, R. S.; Nicolelis, M. A. L. *Nature Neuroscience* **1999**, *2*(7), 664–670.

13. Hochberg, L. R.; Serruya, M. D.; Friehs, G. M.; Mukand, J. A.; Saleh, M.; Caplan, A. H.; Branner, A.; Chen, D.; Penn, R. D.; Donoghue, J. P. *Nature* **2006**, *442*(7099), 164–171.

14. Jog, M.; Connolly, C.; Kubota, Y.; Iyengar, D.; Garrido, L.; Harlan, R.; Graybiel, A. *J. Neurosci. Methods* **2002**, *117*, 141-152.

15. HajjHassan, M.; Chodavarapu, V.; Musallam, S. *Sensors* **2008**, *8*, 6704-6726.

16. Kipke, D. R.; Vetter, R.; Williams, J.; Hetke, J. *IEEE Trans. Neural Syst. Rehabil. Eng.* **2003**, *11*, 151-155.

17. Normann, R.; Maynard, E.; Rousche, P.; Warren, D. *Vision Res.* **1999**, *39*, 2577-2587.

18. Polikov, V.; Tresco, P.; Reichert, W. *J. Neurosci. Methods* **2005**, *148*, 1-18.

19. Gilletti, A.; Muthuswamy, J. *J. Neural Eng.* **2006**, *3*, 189-195.

20. Seymour, J. P.; Kipke, D. R. *Biomaterials* **2007**, *28*, 3594-3607.

21. Najafi, K. *IEEE Engineering in Medicine and Biology Magazine* **1994**, *13*(3), 375–387.

22. Robinson, D. *Proceedings of the IEEE* **1968**, *56*(6), 1065–1071.

23. Skrzypek, J.; Keller, E. *IEEE Transactions on Biomedical Engineering* **1975**, *BME-22*(5), 435–437.

24. Schmidt, E. M.; Bak, M. J.; Christensen, P. *Journal of Neuroscience Methods* **1995**, *62*(1-2), 89–92.

25. Wise, K.; Anderson, D.; Hetke, J.; Kipke, D.; Najafi, K. *Proceedings of the IEEE* **2004**, *92*(1), 76–97.

26. Timko, B. P.; Cohen-Karni, T.; Yu, G.; Qing, Q.; Tian, B.; Lieber, C. M. *Nano Lett.* **2009**, *9*, 914-918.

27. Kim, D.; Viventi, J.; Amsden, J. J.; Xiao, J.; Vigeland, L.; Kim, Y.; Blanco, J. A.; Panilaitis, B.; Frechette, E. S.; Contreras, D.; Kaplan, D. L.; Omenetto, F. G.; Huang, Y.; Hwang, K.; Zakin, M. R.; Litt, B.; Rogers, J. A. *Nat. Mater.* **2010**, *9*, 511-517.

28. Hollenberg, B. A.; Richards, C. D.; Richards, R.; Bahr, D. F.; Rector, D. M. *Journal of Neuroscience Methods***2006**, *153*(1), 147–153.

29. Rousche, P.; Pellinen, D.; Pivin, D.; Williams, J.; Vetter, R.; Kipke, D. R. *IEEE Trans. on Biomed. Eng.* **2001**, *48*, 361-371.

30. Khodagholy, D.; Gelinas, J. N.; Thesen, T.; Doyle, W.; Devinsky, O.; Malliaras, G. G.; Buzsaki, G. *Nat. Neurosci.* **2015**, *18*, 310-315.

31. Xu, B.; Akhtar, A.; Liu, Y.; Chen, H.; Yeo, W.-H.; Park, S. I.; Boyce, B.; Kim, H.; Yu, J.; Lai, H.-Y.; Jung, S.; Zhou, Y.; Kim, J.; Cho, S.; Huang, Y.; Bretl, T.; Rogers, J. A. *Advanced Materials* **2015**, *28*(22), 4462–4471.

32. Rivnay, J.; Wang, H.; Fenno, L.; Deisseroth, K.; Malliaras, G. G. *Sci. Adv.* **2017**, *3*, e1601649.

33. Duan, X.; Fu, T. M.; Liu, J.; Lieber, C. M. *Nano Today* **2013**, *8*, 351-373.

34. Tian, B; Lieber, C. M. *Annu. Rev. Anal. Chem.* **2013**, *6*, 31-51.

35. Duan, X.; Lieber, C. M. *Nano Res*. **2015**, *8*, 1-22.

36. Zhang, A.; Lieber, C. M. *Chem. Rev*. **2016**, *116*, 215-257.

37. Zhou, W.; Dai, X.; Lieber, C. M. *Rep. Prog. Phys*. **2017**, *80*, 016701.

38. Tian, B.; Cohen-Karni, T.; Qing, Q.; Duan, X.; Xie, P.; Lieber, C. M. *Science* **2010**, *9*, 830-834.

39. Qing, Q.; Jiang, Z.; Xu, L.; Gao, R.; Mai, L.; Lieber, C. M. *Nature Nanotechnol.* **2014**, *9*, 142-147.

40. Duan, X.; Gao, R.; Xie, P.; Cohen-Karni, T.; Qing, Q.; Choe, H. S.; Tian, B.; Jiang, X.; Lieber, C. M. *Nat. Nanotechnol.* **2012**, *7*, 174-179.

41. Xie, C.; Hanson, L.; Cui, Y.; Cui, B. *Proc. Natl. Acad. Sci. U. S. A.* **2011**, *108*, 3894-3899.

42. Hanson, L.; Zhao, W.; Lou, H.; Lin, Z. C.; Lee, S. W.; Chowdary, P.; Cui, Y.; Cui, B. *Nat. Nanotechnol.* **2015**, *10*, 554-562.

43. Xie, X.; Xu, A. M.; Angle, M. R.; Tayebi, N.; Verma, P.; Melosh, N. A. *Nano Lett.* **2013**, *13*, 6002-6008.

44. Kim, D. H.; Lu, N.; Ma, R.; Kim, Y.; Kim, R.; Wang, S.; Wu, J.; Won, S. M.; Tao, H.; Islam, A.; Yu, K. J.; Kim, T.; Chowdhury, R.; Ying, M.; Xu, L.; Li, M.; Chung, H.; Keum, H.; McCormick, M.; Liu, P.; Zhang, Y.; Omenetto, F. G.; Huang, Y.; Coleman, T.; Rogers, J. A. *Science* **2011**, *333*, 838-843.

45. Kim, D.; Ghaffari, R.; Lu, N.; Rogers, J. A. *Annua. Rev. Biomed. Eng.* **2012**, *14*, 113-128.

46. Choi, C.; Choi, M. K.; Hyeon, T.; Kim, D. *Chem. Nano. Mat.* **2016**, *2*, 1006-1017.

47. Xie, C.; Liu, J.; Fu, T.; Dai, X.; Zhou, W.; Lieber, C. M. *Nat. Mater.* **2015**, *14*, 1286-1292.

48. Liu, J.; Fu, T.; Cheng, Z.; Hong, G.; Zhou, T.; Jin, L.; Duvvuri, M.; Jiang, Z.; Kruskal, P.; Xie, C.; Suo, Z.; Fang, Y.; Lieber, C. M. *Nat. Nanotechnol.* **2015**, *10*, 629-637.

49. Hong, G.; Fu, T.; Zhou, T.; Schuhmann, T. G.; Huang, J.; Lieber, C. M. *Nano Lett.* **2015**, *15*, 6979-6984.

50. Zhou, T.; Hong, G.; Fu, T.; Yang, X.; Schuhmann, T. G.; Viveros, R. D.; Lieber, C. M. *PNAS*, **2017**, *114*, 5894-5899

51. Hwang, S.; Tao, H.; Kim, D.; Cheng, H.; Song, J.; Rill, E.; Brenckle, M. A.; Panilaitis, B.; Won, S. M.; Kim, Y.; Song, Y. M.; Yu, K. J.; Ameen, A.; Li, R.; Su, Y.; Yang, M.; Kaplan, D. L.; Zakin, M. R.; Slepian, M. J.; Huang, Y.; Omenetto, F. G.; Rogers, J. A. *Science* **2012**, *337*, 1640-1644.

52. Kim, T.; McCall, J. G.; Jung, Y. H.; Huang, X.; Siuda, E. R.; Li, Y.; Song, J.; Song, Y. M.; Pao, H. A.; Kim, R.; Lu, C.; Lee, S. D.; Song, I.; Shin, G.; Al-Hasani, R.; Kim, S.; Tan, M. P.; Huang, Y.; Omenetto, F. G.; Rogers, J. A.; Bruchas, M. R. *Science* **2013**, *340*, 211-216.

53. Koh, A.; Gutbrod, S. R.; Meyers, J. D.; Lu, C.; Webb, R. C.; Shin, G.; Li, Y.; Kang, S.; Huang, Y.; Efimov, I. R.; Rogers, J. A. *Adv. Healthc. Mater.* **2016**, *5*, 373-381.

54. Luan, L.; Wei, X.; Zhao, Z.; Siegel, J. J.; Potnis, O.; Tuppen, C. A.; Lin, S.; Kazmi, S.; Fowler, R. A.; Holloway, S.; Dunn, A. K.; Chitwood, R. A.; Xie, C. *Sci. Adv.* **2017**, *3*, e1601966.

55. Hwang, S.; Lee, C. H.; Cheng, H.; Jeong, J.; Kang, S.; Kim, J.; Shin, J.; Yang, J.; Liu, Z.; Ameer, G. A.; Haung, Y.; Rogers, J. A. *Nano Lett.* **2015**, *15*, 2801-2808.

56. Gunatillake, P.; Mayadunne, R.; Adhikari, R. *Biotechnol. Annu. Rev.* **2006**, *2*, 301-347.

57. Kim, U. J.; Park, J.; Kim, H.; Wada, M.; Kaplan, D. *Biomaterials* **2005**, *26*, 2775-2785.

58. Nair, L. S.; Laurencin, C. T. *Prog. Polym. Sci.* **2007**, *32*, 762-798.

59. Kurland, N. E.; Dey, T.; Wang, C.; Kundu, S. C.; Yadavalli, V. K. *Adv. Mater.* **2014**, *26*, 4431-4437.

60. Khilwani, R.; Gilgunn, P. J.; Kozai, T. D. Y.; Ong, X. C.; Korkmaz, E.; Gunalan, P. K.; Cui, X. T.; Fedder, G. K.; Ozdoganlar, O. B. *Biomed. Microdevices* **2016**, *18*, 97.

61. Barz, F.; Ruther, P.; Takeuchi, S.; Paul, O. Flexible silicon-polymer neural probe rigidified by dissolvable insertion vehicle for high-resolution neural recording with improved duration, Proceedings of The 28th International Conference on Micro Electro Mechanical Systems, Estoril, Portugal, Jan 18-22, 2015; IEEE, 2015; pp. 636-639.

62. Kozai, T. D. Y.; Gugel, Z.; Li, X.; Gilgunn, P. J.; Khilwani, R.; Ozdoganlar, O. B.; Fedder, G. K.; Weber, D. J.; Cui, X. T. *Biomaterials* **2014**, *35*, 9255-9268.

63. Yin, L.; Cheng, H.; Mao, S.; Haasch, R.; Liu, Y.; Xie, X.; Hwang, S.; Jain, H.; Kang, S.; Su, Y.; Li, R.; Huang, Y.; Rogers, J. A. *Adv. Funct. Mater.* **2014**, *24*, 645-658.

64. Hwang, S.; Park, G.; Cheng, H.; Song, J.; Kang, S.; Yin, L.; Kim, J.; Omenetto, F. G.; Huang, Y.; Lee, K.; Rogers, J. A. *Adv. Mater.* **2014**, *26*, 1992-2000.

65. Shioda, R.; Reinach, P. S.; Hisatsune, T.; Miyamoto, Y. *Invest. Ophthalmol. Vis. Sci.* **2002***, 43,* 2916-2922.

66. Veloso, D.; Guynn, R. W.; Oskarsson, M.; Veech, R. L. *J. Biol. Chem.* **1973**, *248*, 4811-4819.

67. Taylor, J.; Vigneron, D.; Muphyboesch, J.; Nelson, S.; Kessler, H.; Coia, L.; Curran, W.; Brown, T. *Proc. Natl. Acad. Sci. U. S. A.* **1991**, *88*, 6810-6814.

68. Sato, Y.; Fukuda, J. *Clin. Calcium.* **2004**, *14*, 50-57.

69. Watanabe, M; Wu, J. R.; Li, C. Z.; Okada, T. *Exp. Clin. Cardiol.* **2004**, *9*, 181-185.

70. Dribben, W. H.; Eisenman, L. N.; Mennerick, S. *Cell Death and Dis.* **2010**, *1*, e63.

71. Fu, T. M.; Hong, G.; Zhou, T.; Schuhmann, T. G.; Viversos, R. D.; Lieber, C. M. *Nat. Methods.* **2016**, *13*, 875-882.

72. Chesik, D.; Glazengburg, L.; Keyser, J. D.; Wilczak, N. *J. Neurochem.* **2007**, *100*, 1555-1564.

73. Klokholm, E.; Berry, B. *J. Electrochem. Soc.* **1968**, *8*, 823-826.

74. Tian, B.; Liu, J.; Dvir, T.; Jin, L.; Tsui, J. H.; Qing, Q.; Suo, Z.; Langer, R.; Kohane, D. S.; Lieber, C. M. *Nat. Mater.* **2012**, *11*, 986-994.

75. Harrison, R.; Kier, R.; Chestek, C.; Gilja, V.; Nuyujukian, P.; Ryu, S.; Greger, B.; Solzbacher, F.; Shenoy, K. *IEEE Transactions on Neural Systems and Rehabilitation Engineering* **2009**, *17*(4), 322–329.

76. Sodagar, A. M.; Perlin, G. E.; Yao, Y.; Wise, K. D.; Najafi, K. *TRANSDUCERS 2007 - 2007 International Solid-State Sensors, Actuators and Microsystems Conference* **2007**.

77. Yeager, D. J.; Holleman, J.; Prasad, R.; Smith, J. R.; Otis, B. P. *IEEE Transactions on Biomedical Circuits and Systems***2009**, *3*(6), 379–387.

78. Schwerdt, H. N.; Xu, W.; Shekhar, S.; Abbaspour-Tamijani, A.; Towe, B. C.; Miranda, F. A.; Chae, J. *Journal of Microelectromechanical Systems***2011**, *20*(5), 1119–1130.

79. Qing, Q.; Pal, S. K.; Tian, B.; Duan, X.; Timko, B. P.; Cohen-Karni, T.; Murthy, V. N.; Lieber, C. M. *Proceedings of the National Academy of Sciences* **2010**, *107*(5), 1882–1887.

80. Cohen-Karni, T.; Timko, B. P.; Weiss, L. E.; Lieber, C. M. *Proceedings of the National Academy of Sciences* **2009**, *106*(18), 7309–7313.

81. Patolsky, F.; Lieber, C. M. *Materials Today* **2005**, *8*(4), 20–28.

82. Freer, E. M.; Grachev, O.; Duan, X.; Martin, S.; Stumbo, D. P. *Nature Nanotechnology* **2010**, *5*(8), 625–625.

83. Zutic, I.; Fabian, J.; Sarma, S. D. *Rev. Mod. Phys.* **2004**, *76*, 323-410.

84. Parkin, S. S. P.; Mauri, D. *Physical Review B* **1991**, *44*(13), 7131–7134.

85. Rifai, D.; Abdalla, A.; Ali, K.; Razali, R. *Sensors* **2016**, *16*(12), 298.

86. Ventura, J.; Sousa, J.; Freitas, P.; Veloso, A. *Journal of Magnetism and Magnetic Materials* **2004**, *272-276*, 1892–1894.

87. Egelhoff, W. F.; Chen, P. J.; Powell, C. J.; Parks, D.; Serpa, G.; Mcmichael, R. D.; Martien, D.; Berkowitz, A. E. *Journal of Vacuum Science & Technology B: Microelectronics and Nanometer Structures* **1999**, *17*(4), 1702.

88. Djamal, M.; Ramli. *Procedia Engineering* **2012**, *32*, 60–68.

89. Julliere, M. *Physics Letters A* **1975**, *54*(3), 225–226.

90. Miyazaki, T.; Tezuka, N. *Journal of Magnetism and Magnetic Materials* **1995**, *139*(3).

91. Moodera, J. S.; Kinder, L. R.; Wong, T. M.; Meservey, R. *Physical Review Letters* **1995**, *74*(16), 3273–3276.

92. Tian, Y.; Yan, S. *Science China Physics, Mechanics and Astronomy* **2012**, *56*(1), 2–14.

93. Mathon, J.; Umerski, A. *Physical Review B* **2001**, *63*(22).

94. Yuasa, S.; Nagahama, T.; Fukushima, A.; Suzuki, Y.; Ando, K. *Nature Materials* **2004**, *3*(12), 868–871.

95. Parkin, S. S. P.; Kaiser, C.; Panchula, A.; Rice, P. M.; Hughes, B.; Samant, M.; Yang, S.-H. *Nature Materials* **2004**, *3*(12), 862–867.

96. Ikeda, S.; Hayakawa, J.; Ashizawa, Y.; Lee, Y. M.; Miura, K.; Hasegawa, H.; Tsunoda, M.; Matsukura, F.; Ohno, H. *Applied Physics Letters* **2008**, *93*(8), 082508.

97. Reohr, W.; Honigschmid, H.; Robertazzi, R.; Gogl, D.; Pesavento, F.; Lammers, S.; Lewis, K.; Arndt, C.; Lu, Y.; Viehmann, H.; Scheuerlein, R.; Wang, L.-K.; Trouilloud, P.; Parkin, S.; Gallagher, W.; Muller, G. *IEEE Circuits and Devices Magazine* **2002**, *18*(5), 17–27.

98. Datta, S.; Das, B. *Applied Physics Letters* **1990**, *56*(7), 665–667.

99. Bychkov, Y. A.; Rashba, E. I. *Journal of Physics C: Solid State Physics***1984**, *17*(33), 6039–6045.

100. Wang, G.; Wang, Z.; Klein, J.-O.; Zhao, W. *IEEE Transactions on Magnetics* **2017**, *53*(11), 1–6.

101. Schumacher, B. *Physical Review A* **1995**, *51*(4), 2738–2747.

102. Steane, A. *Reports on Progress in Physics* **1998**, *61*(2), 117–173.

103. Monroe, C. R.; Schoelkopf, R. J.; Lukin, M. D. *Scientific American* **2016**, *314*(5), 50–57.

104. Schmied, R.; Bancal, J.-D.; Allard, B.; Fadel, M.; Scarani, V.; Treutlein, P.; Sangouard, N. *Science* **2016**, *352*(6284), 441–444.

105. Feynman, R. P. *International Journal of Theoretical Physics* **1982**, *21*(6-7), 467–488.

106. Benioff, P. *Journal of Statistical Physics* **1982**, *29*(3), 515–546.

107. Shor, P. W. *SIAM Journal on Computing* **1997**, *26*(5), 1484–1509.

108. Shor, P. W. *Physical Review A* **1995**, *52*(4).

109. Cory, D. G.; Price, M. D.; Maas, W.; Knill, E.; Laflamme, R.; Zurek, W. H.; Havel, T. F.; Somaroo, S. S. *Physical Review Letters* **1998**, *81*(10), 2152–2155.

110. Jones, J. A.; Mosca, M.; Hansen, R. H. *Nature* **1998**, *393*(6683), 344–346.

111. Saffman, M. *Journal of Physics B: Atomic, Molecular and Optical Physics* **2016**, *49*(20), 202001.

112. Piotrowicz, M. J.; Lichtman, M.; Maller, K.; Li, G.; Zhang, S.; Isenhower, L.; Saffman, M. *Physical Review A* **2013**, *88*(1).

113. Saffman, M.; Walker, T. G. *Physical Review A* **2005**, *72*(2).

114. Cirac, J. I.; Zoller, P. *Physical Review Letters* **1995**, *74*(20), 4091–4094.

115. Kim, J. *Physics***2014**, *7*.

116. Harty, T. E. P.; Allcock, D. T. C.; Ballance, C. J.; Guidoni, L.; Janacek, H. A.; Linke, N. M.; Stacey, D. N.; Lucas, D. M. *Physical Review Letters***2014**, *113*(22).

117. You, J. Q.; Nori, F. *Nature* **2011**, *474*(7353), 589–597.

118. Ladd, T. D.; Jelezko, F.; Laflamme, R.; Nankamura, Y.; Monroe, C.; O'Brien, J. L. *Nature* **2010**, *464*, 45-53.

119. Unruh, W. G. *Phys. Rev. A* **1994**, *51*, 992-997.

120. Hanson, R.; Awschalom, D. *Nature* **2008**, *453*, 1043-1049.

121. Loss, D.; DiVincenzo, D. P. *Phys. Rev. A*, **1998**, *57*, 120-126.

122. Hayashi, T.; Fujisawa, T.; Cheong, H. D.; Jeong, Y. H.; Hirayama, Y. *Phys. Rev. Lett.* **2003**, *91*, 226804.

123. Petta, J. R.; Johnson, A. C.; Taylor, J. M.; Laird, E. A.; Yacoby, A.; Lukin, M. D.; Marcus, C. M.; Hanson, M. P.; Gossard, A. C. *Science* **2005**, *309*, 2108-2184.

124. Markham, M.; Dodson, J.; Scarsbrook, G.; Twitchen, D.; Balasubramanian, G.; Jelezko, F.; Wrachtrup, J. *Diamond and Related Materials* **2011**, *20*(2), 134–139.

125. Reynhardt, E. C.; High, G. L.; van Wyk, J. A. *J. Chem. Phys.***1998**, *109*, 8471-8477.

126. Gruber, A.; Drabenstedt, A.; Tietz, C.; Fleury, L.; Wrachtrup, J.; von Borczyskowski, C. *Science* **2012**, *276*, 2012–2014.

127. Jelezko, F.; Popa, I.; Gruber, A.; Wrachtrup, J. *Appl. Phys. Lett.* **2002**, *81*, 2160–2162.

128. Jelezko, F.; Gaebel, T.; Popa, I.; Gruber, A.; Wrachtrup, J. *Phys. Rev. Lett.* **2004**, *92*, 76401.

129. Jelezko, F.; Gaebel, T.; Popa, I.; Domhan, M.; Gruber, A.; Wrachtrup, J. *Phys. Rev. Lett.* **2004**, *93*, 130501.

130. Harrison, J.; Sellars, M. J.; Manson, N.B.; *JOL* **2004**, *107*, 245-248.

131. Gurudev Dutt, M. V.; Childress, L.; Jiang, L.; Togan, E.; Maze, J.; Jelezko, F.; Zibrov, A. S.; Hemmer, P. R.; Lukin, M. D. *Science* **2007**, *316*, 1312–1316.

132. Kimura, T.; Hamrle, J.; Otani, Y.; Tsukagoshi, K.; Aoyagi, Y. *Appl. Phys. Lett.* **2004**, *85*, 3501-3503.

133. Valenzuela, S. O.; Tinkham, M. *Appl. Phys. Lett.*, **2004**, *85*, 5914-5916.

134. Buhrman, R. A. *Spin Electronics***2004**, 35–48.

135. Wolf, S. A. *Science***2001**, *294*(5546), 1488–1495.

136. Restrepo, O. D.; Windl, W.; *Phys. Rev. Lett.* **2012**, *109*, 166604.

137. Doherty, M. W.; Meriles, C. A.; Alkauskas, A.; Fedder, H.; Sellars, M. J.; Manson, N. B. *Phys. Rev. A*, **2016**, *6*, 041035.

138. Cardellino, J.; Scozzaro, N.; Herman, M.; Berger, A. J.; Zhang, C.; Fong, K. C.; Jayaprakash, C.; Pelekhov, D. V.; Hammel, P. C. *Nature Nanotechnology***2014**, *9*(5), 343–347.

139. Bass, J.; Pratt, W. P. *J. Phys. Condens. Matter* **2007**, *19*, 183201.

140. Ji, Y.; Hoffmann, A.; Jiang, J. S.; Pearson, J. E.; Bader, S. D. *J. Phys. D*, **2007**, *40*, 1280-1284.

APPENDIX A

CO-AUTHORS AGREEMENT ON USING PUBLISHED WORK

Part of chapter 2 in this dissertation was published as Scalable Fabrication Framework of Implantable Ultrathin and Flexible Probes with Biodegradable Sacrificial Layers in Nano Letters (Jiao et al., 2017). All co-authors have granted their permission of using the published article in this dissertation.